minerals

MDPI

Article

Geochronology and Geochemistry of Granitoids from the Zhuanshanzi Gold Deposit, Northern Margin of the North China Craton: Implications for Petrogenesis and Tectonic Significance

Xueli Ma [1], Kaituo Shi [2,*], Cailin Wang [1], Kairui Song [1], Hongguang Lv [1] and Xiaolin Liu [1]

[1] School of Resources, Environment and Architectural Engineering, Chifeng University, Chifeng 024000, China
[2] School of Resource Environment and Safety Engineering, University of South China, Hengyang 421001, China
* Correspondence: kaituos@usc.edu.cn

Abstract

During the Late Paleozoic and Early Mesozoic, intensive tectonic and magmatic activity along the northern margin of the North China Craton (NCC) was associated with widespread gold mineralization. This study investigates the petrology, geochemistry, and zircon U–Pb ages of granite porphyry, quartz monzonite, and granite dikes from the Zhuanshanzi gold deposit in the Chifeng–Chaoyang region, central segment of the northern NCC, to constrain the petrogenesis and tectonic evolution. The zircon U–Pb dating yields emplacement ages of 245 ± 3 Ma and 248 ± 3 Ma for the granite porphyry and quartz monzonite, respectively (Early–Middle Triassic), and 364 ± 3 Ma for the granite dikes (Late Devonian). From the Late Devonian to the Early Permian, the study area was an active continental margin characterized by subduction of the Paleo-Asian Ocean beneath the NCC. The Late Devonian granite dikes are peraluminous, high-K calc-alkaline, and adakitic, and likely formed during arc–arc collisions that led to localized crustal thickening. By the Early–Middle Triassic, the Xing'an–Mongolian Orogenic Belt had collided with the NCC, marking the final closure of the Paleo-Asian Ocean. The Early Triassic quartz monzonite is a high-K calc-alkaline, peraluminous C-type adakite, derived from partial melting of thickened lower crust during the late- to post-collisional transition. In contrast, the Middle Triassic granite porphyry exhibits high-K, calc-alkaline, metaluminous A-type granitic affinities, consistent with a low-pressure partial melting of crustal material during post-orogenic extension transitioning to intracontinental rifting. Integrated with previous studies, we conclude that the Zhuanshanzi region records a prolonged evolution from subduction, through arc–arc collision and crustal thickening, to post-orogenic extension and intracontinental rifting of the Paleo-Asian Ocean from the Late Devonian to the Middle Triassic.

Keywords: North China Craton; zircon U–Pb geochronology; geochemistry; Paleo-Asian Ocean; Inner Mongolia; Zhuanshanzi gold deposit

Check for updates

Academic Editor: Simon Paul Johnson

Received: 29 July 2026
Revised: 26 August 2026
Accepted: 27 August 2026
Published: 28 August 2026

Copyright: © 2026 by the authors. Licensee MDPI, Basel, Switzerland. This article is an open access article distributed under the terms and conditions of the Creative Commons Attribution (CC BY) license.

1. Introduction

In China, most orogenic, epithermal, and Carlin-like gold deposits are situated along the reworked margins of major cratonic blocks and within adjacent metasedimentary-dominated fold belts, with three-quarters of gold-only deposits occurring within the margins of the North China Craton (NCC) (Figure 1A) [1]. The NCC preserves ancient rocks as old as ca. 3.8 Ga [2], and remained tectonically stable from ca. 1.85 Ga to 200 Ma [3–5]. However, since ca. 200 Ma, the NCC has experienced frequent magmatic activity and orogenic deformation [6,7]. The destruction of the NCC during the Late Mesozoic not only led

to tectonic reactivation but also made it an important mineral-resource-producing region (Figure 1B) [8–13]. As noted by previous researchers, the Xing'an–Mongolian Orogenic Belt formed during the final closure of the Paleo-Asian Ocean and the amalgamation of the NCC in the Late Permian–Early Triassic [14–18]. Therefore, a thorough understanding of the spatio-temporal relationships and genetic mechanisms of multi-stage magmatic–hydrothermal activity in this orogenic belt is crucial for deciphering the subduction history of the Paleo-Asian Ocean in the north of the NCC and the timing of its final closure [19,20].

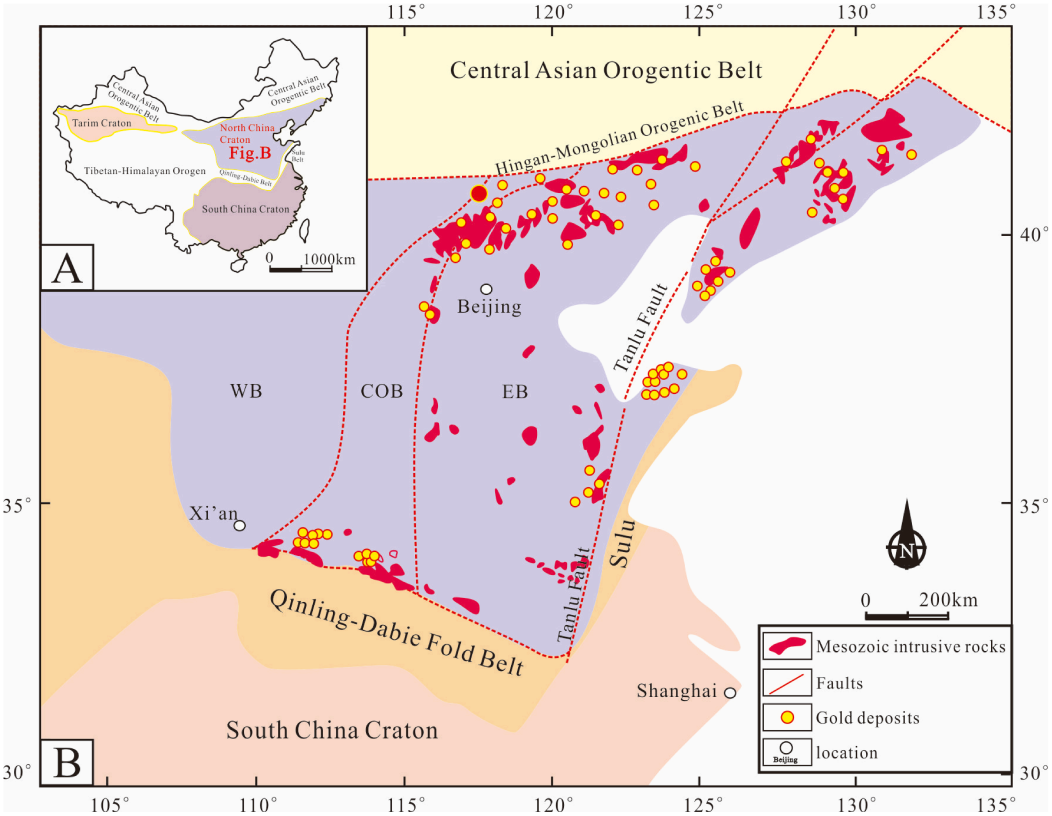


Figure 1. (**A**) Tectonic subdivision of the Chinese continent (modified from [21]). (**B**) Geological map of eastern China, showing the main tectonic elements. Abbreviations: WB—western block; COB (TNCO)—central orogenic belt (Trans-North China Orogen); EB—eastern block. These denote the three-fold tectonic division of the North China Craton (compiled after [22]).

The Chifeng–Chaoyang region, located in the central segment of the northern margin of the NCC, is one of the most important gold metallogenic belts and hosts dozens of medium- to large-sized Au deposits (Figure 2A) [21,23,24]. The Zhuanshanzi deposit, a typical lode gold deposit in the Chifeng–Chaoyang region, contains >18 t Au at an average grade of 10.0 g/t (Figure 2B) [25]. This high-grade resource endowment highlights the exceptional gold potential of the Chifeng–Chaoyang metallogenic belt and underscores the importance of understanding the magmatic–hydrothermal processes controlling such mineralization. Although discovered in the 1950s, the Zhuanshanzi deposit was not systematically explored until 2013, and prior research focused mainly on the general geology [26–28]. Currently, there is no consensus on the source or evolution of the granitoids in this deposit, and their geochronology, geochemical characteristics, and isotopic compositions remain poorly constrained. To address these issues and provide a basis for further research, this paper presents new zircon U–Pb ages and whole-rock geochemical data for the granitoids at Zhuanshanzi, and systematically investigates their petrological classification, geochronology, and petrogenesis. Importantly, this study identifies for the first time the Late Devonian adakitic magmatism in this area, thus extending the known

magmatic history of the northern NCC and providing new insights into the pre-Mesozoic metallogenic setting.

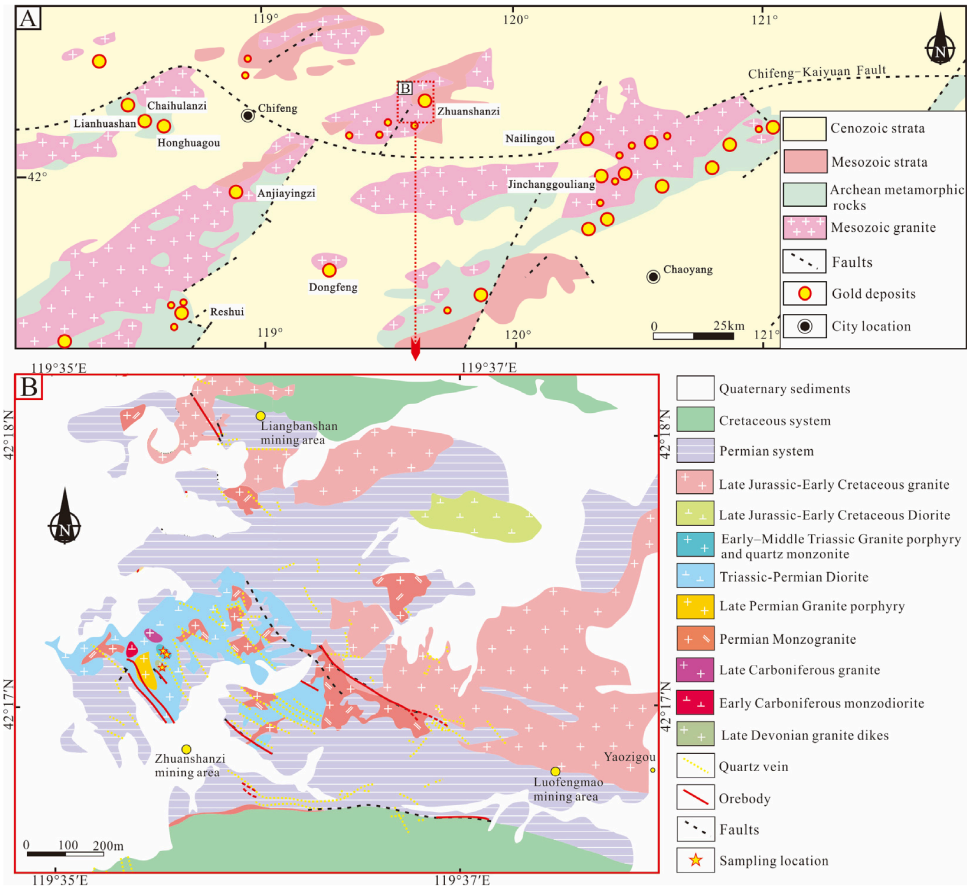


Figure 2. (**A**) Geological map of the Chifeng–Chaoyang region showing the distribution of Mesozoic granites and gold deposits (modified after [21]). (**B**) Geological map of the Zhuanshanzi deposit (modified after [27]).

2. Geological Background

2.1. Regional Geology

The Chifeng–Chaoyang region is located in the northern part of the NCC, south of the Xing'an–Mongolian Orogenic Belt (Figures 1B and 2A). The region experienced the subduction and closure of the Paleo-Asian Ocean during the Paleozoic to Early Mesozoic, and was subsequently overprinted by westward subduction of the Paleo-Pacific Plate since the Mesozoic, resulting in a unique tectonic framework [29–32]. The Precambrian basement in this region is dominated by a gneissic complex and metamorphic supracrustal rocks, consisting of sedimentary and volcanic sequences, together with TTG gneisses that have undergone varying degrees of migmatization (Figure 2A). The Paleozoic strata, represented by Permian successions, consist of a suite of metasedimentary rocks derived from limestone (including garnet–diopside marble, epidote–tremolite hornfels, and garnet–epidote marble) and a suite of volcanic rocks [27,30]. The Mesozoic strata, represented by Early Cretaceous deposits, comprise an assemblage of conglomerate, rhyolite, and trachyte [27]. The structural framework of this region is dominated by NE-striking faults, which control the distribution of Yanshanian intrusions, most notably exemplified by the Chifeng–Kaiyuan Fault (Figure 2A). The Late Paleozoic granitoids, predominantly represented by a porphyritic biotite granite batholith, are distributed in the southern part of this region and were emplaced during the late Hercynian (Figure 2A) [33]. The Mesozoic granitoid com-

plexes consist predominantly of granite, granodiorite, diorite, and syenogranite, and were emplaced from the Triassic to the Early Cretaceous [10,20]. The regional gold mineralization is predominantly of quartz-vein type, with subordinate altered-rock-type mineralization, and is hosted in Archean metamorphic rocks or Mesozoic granites [21].

2.2. Deposit Geology

The Zhuanshanzi gold deposit (119°35′ E, 42°18′ N; Figure 2B) is located in Aohan Banner, approximately 50 km east of Chifeng City, Inner Mongolia. The exposed stratigraphic sequence consists predominantly of the Lower Permian Yujiabeigou Formation, the Upper Cretaceous Sunjiawan Formation, and Quaternary sediments, with minor exposure of the Upper Jurassic Baiyin'gaolao Formation (Figure 2B). The Yujiabeigou Formation is distributed in the central and eastern parts of the ore deposit and consists of a suite of shallow marine, coastal carbonate and clastic sedimentary strata with a thickness of 1500–2000 m. The ore veins are mainly hosted in the Yujiabeigou Formation along the E- and NE-trending structures. The Zhuanshanzi pluton comprises a suite of medium- to coarse-grained granodiorite, quartz monzonite, granite dike, and granite porphyry (Figure 2B) intruding into the Permian strata.

2.3. Petrography

After detailed field investigation, representative samples of the Early–Middle Triassic granite porphyry, quartz monzonite, and Late Devonian granite dikes were collected from outcrops and drill holes for detailed studies (Figure 3A–C). The granite porphyry is massive, medium- to fine-grained, pink in color, and consists of 80%–85% felsic groundmass and 15%–20% phenocrysts that are predominantly alkali feldspar with minor plagioclase (Figure 3D). The quartz monzonite consists of plagioclase (40%–50%), quartz (5%–20%), K-feldspar (3%–40%), amphibole (~15%), and biotite (~5%) (Figure 3E). The granite dikes have an aplitic texture and are composed mainly of K-feldspar (~45%), plagioclase (~20%), and quartz (~30%), with minor biotite and muscovite (Figure 3F).

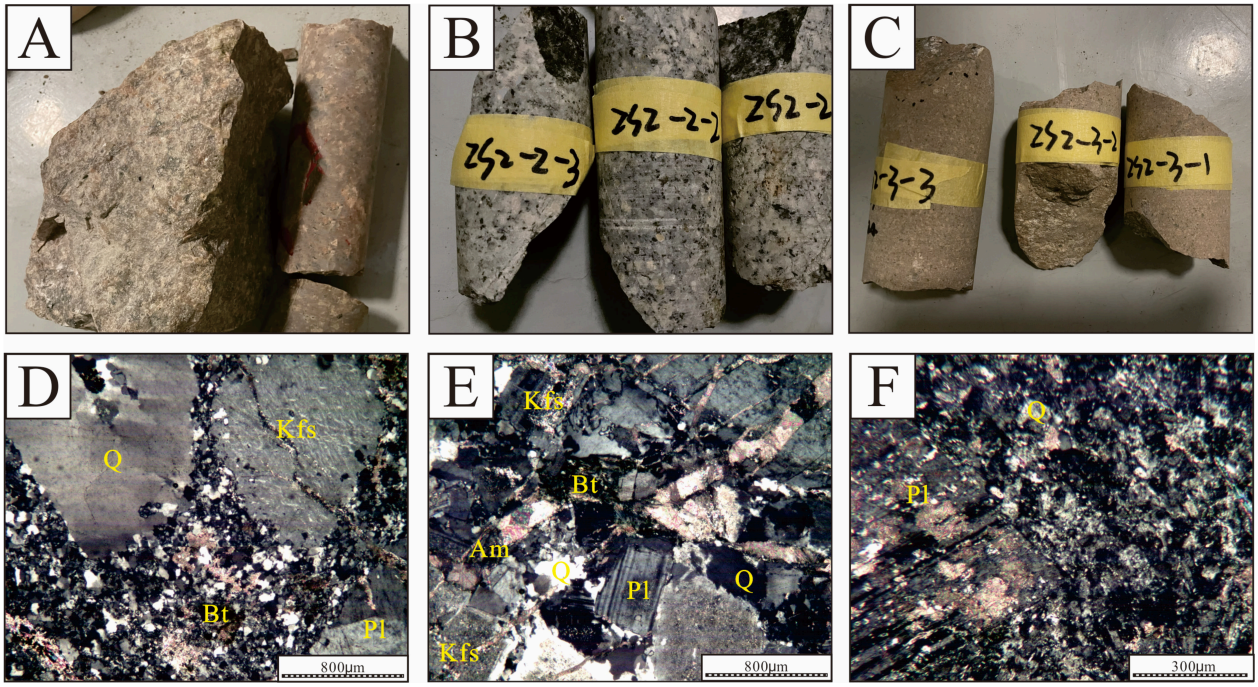


Figure 3. (**A**–**C**) Hand specimens and (**D**–**F**) photomicrographs of the Early–Middle Triassic granite porphyry, quartz monzonite, and Late Devonian granite dikes from the Zhuanshanzi deposit. Mineral abbreviations: Q = quartz; Kfs = K-feldspar; Pl = plagioclase; Bt = biotite; Am = amphibole.

3. Analytical Methods

3.1. LA–ICP–MS Zircon U–Pb Dating

Zircon grains were separated from the granite porphyry (ZSZ-1), quartz monzonite (ZSZ-2), and granite dikes (ZSZ-3) using conventional heavy liquid and magnetic separation techniques, and were then hand-picked under a binocular microscope at the Langfang Regional Geological Survey, Hebei, China. Detailed analytical procedures and instrumental settings are given in [34].

The zircon U–Pb dating was performed using an Agilent 7500c quadrupole ICP–MS (Agilent, Santa Clara, CA, USA) coupled to a 193 nm ArF excimer laser ablation system (COMPexPro 102, Coherent, Dieburg, Germany) at the Key Laboratory of Mineral Resources Evaluation in Northeast Asia, Ministry of Natural Resources, China. The trace element concentrations were calibrated using NIST 610 glass as the external standard and Si as the internal standard. The U–Pb isotopic fractionation was corrected by normalization to zircon standard 91500 [35]. The Plešovice zircon standard (337 Ma) [36] was analyzed as a secondary standard to monitor the accuracy of the obtained ages. The laser spot size was 32 μm, with a laser energy density of 10 J/cm^2 and a repetition rate of 8 Hz. Each analysis consisted of a 30 s background measurement, 30 s of sample ablation, and 2 min of post-ablation flushing. The ablated material was transported to the ICP–MS by a high-purity helium carrier gas (1.15 L/min). Argon make-up gas (0.60 L/min) was added to the carrier flow to improve signal stability. The dwell times were 20 ms for ^{204}Pb, ^{206}Pb, ^{207}Pb, and ^{208}Pb; 15 ms for ^{232}Th and ^{238}U; 20 ms for ^{49}Ti; and 6 ms for all other elements [34].

The trace element concentrations and U–Pb isotope ratios of zircons were calculated using GLITTER 4.5 software. The concordia diagrams and weighted mean ages were constructed using Isoplot/Ex 3.0 [37]. The analytical data are presented on U–Pb concordia diagrams with 2σ errors, and the weighted mean ages are quoted at a 95% confidence level. A common Pb correction was performed following the procedures described by [38].

3.2. Whole-Rock Geochemical Analyses

Four granite porphyry, three quartz monzonite, and three granite dike samples were chosen for whole-rock geochemical analyses. All the samples selected for geochemical analysis were fresh, without visible hydrothermal alteration. The petrographic observations indicated that the primary igneous minerals (plagioclase, K-feldspar, quartz, biotite, and amphibole) were well preserved and showed no signs of sericitization, chloritization, or carbonatization.

The rock samples were crushed in a steel jaw crusher and then pulverized to 200 mesh in an agate mill at ALS Minerals–ALS Chemex, Guangzhou, China. The major element concentrations were determined by X-ray fluorescence (ME-XRF26d), and the trace element concentrations were measured by ICP-MS (ME-MS81). The syenite reference material SARM-2 was analyzed to monitor the data quality for the major elements, while the uranium reference material OREAS 120 was analyzed concurrently to assess the quality of trace element data. The analytical precision, expressed as the relative standard deviation (RSD), was better than 5% for the major elements and 10% for the trace elements. The loss on ignition (LOI) was determined by heating the sample in a pre-ignited silica crucible at 1000 °C for one hour and recording the percentage weight loss.

4. Results

4.1. Zircon U–Pb Age

Seventeen zircon grains from the granite porphyry (ZSZ-1) are predominantly colorless and prismatic, ranging from 70 to 160 μm in length, with aspect ratios of 1:1 to 3:1. Most grains are euhedral and exhibit igneous oscillatory zoning (Figure 4A) [39]. The zircon grains have Th and U contents of 106.0–644.0 ppm and 83.4–771.0 ppm (Table 1), respectively, with Th/U ratios of 0.71–1.52, consistent with an igneous origin [40]. Twenty-three spot analyses yielded $^{206}Pb/^{238}U$ ages ranging from 230 ± 3 Ma to 255 ± 5 Ma (Figure 4A), yielding a weighted mean age of 245 ± 3 Ma (MSWD = 3.7; Figure 4B). This is interpreted as the crystallization age of the granite porphyry.

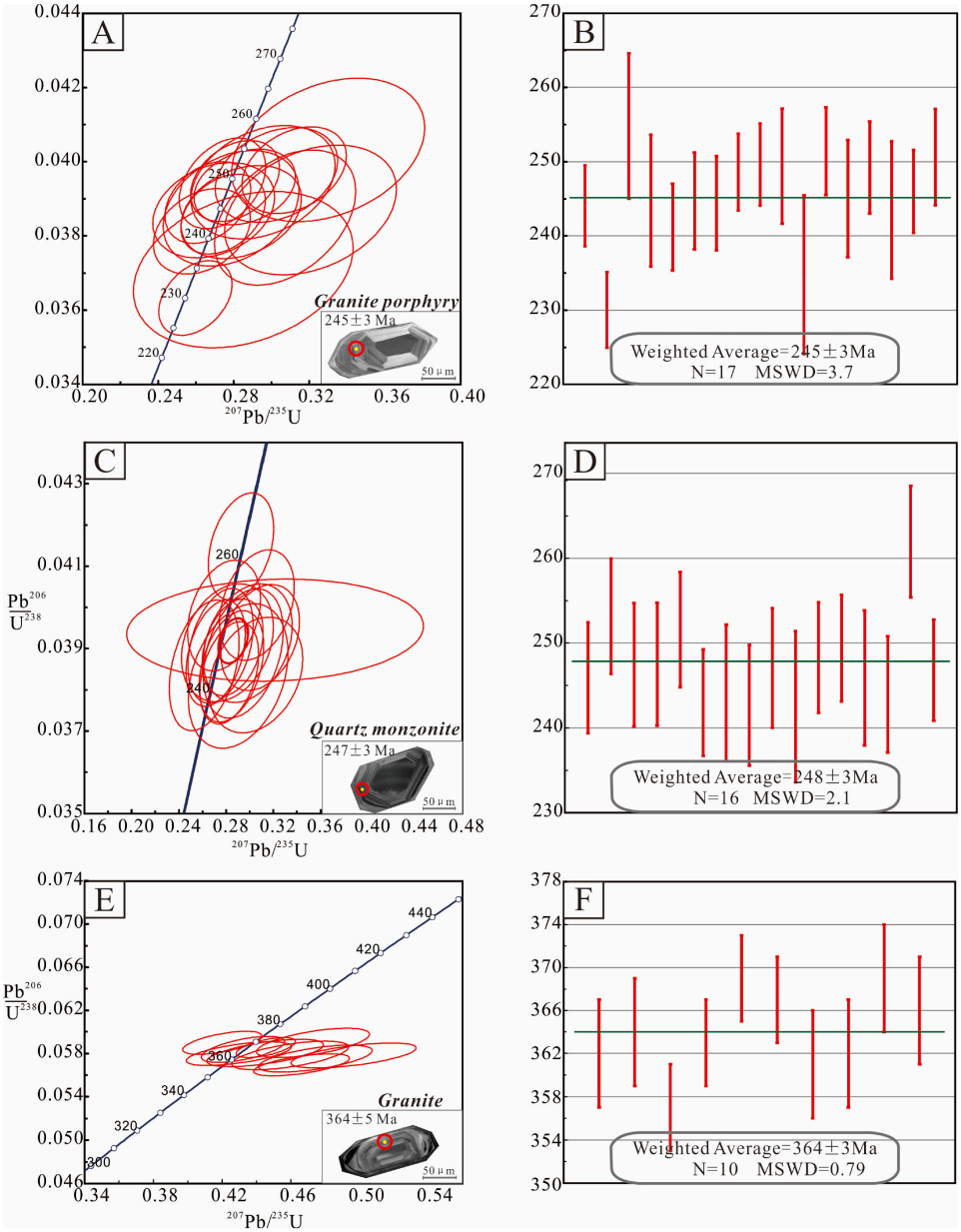


Figure 4. (**A**,**B**) Zircon U–Pb concordia diagram and weighted mean age plot for the Zhuanshanzi granite porphyry. (**C**,**D**) Zircon U–Pb concordia diagram and weighted mean age plot for the Zhuanshanzi quartz monzonite. (**E**,**F**) Zircon U–Pb concordia diagram and weighted mean age plot for the Zhuanshanzi granite dikes.

Table 1. LA-ICP-MS zircon U–Pb dating results for the granite porphyry (ZSZ-1), quartz monzonite (ZSZ-2), and granite dike (ZSZ-3) samples from the Zhuanshanzi deposit.

					Isotopic Ratios						Ages (Ma)					
	($\omega_B/10^{-6}$)				$^{207}Pb/^{206}Pb$		$^{207}Pb/^{235}U$		$^{206}Pb/^{238}U$		$^{207}Pb/^{206}Pb$		$^{207}Pb/^{235}U$		$^{206}Pb/^{238}U$	
Sample No.	**Pb**	**Th**	**U**	**Th/U**	**Ratios**	**1σ**	**Ratios**	**1σ**	**Ratios**	**1σ**	**Ratios**	**1σ**	**Ratios**	**1σ**	**Ratios**	**1σ**
ZSZ-1-1	99	554	502	1.10	0.0516	0.0018	0.2744	0.0091	0.0386	0.0004	333	78	246	7	244	3
ZSZ-1-2	111	644	771	0.84	0.0517	0.0015	0.2597	0.0079	0.0363	0.0004	333	67	234	6	230	3
ZSZ-1-3	19.8	106	83.4	1.27	0.0614	0.0042	0.3300	0.0209	0.0403	0.0008	654	146	290	16	255	5
ZSZ-1-4	29.6	163	116	1.41	0.0618	0.0037	0.3206	0.0186	0.0387	0.0007	665	128	282	14	245	4
ZSZ-1-5	90	531	350	1.52	0.0506	0.0021	0.2631	0.0105	0.0381	0.0005	233	98	237	8	241	3
ZSZ-1-6	39.2	207	202	1.03	0.0506	0.0025	0.2694	0.0132	0.0387	0.0005	220	115	242	11	245	3
ZSZ-1-7	69	354	333	1.06	0.0535	0.0025	0.2840	0.0130	0.0386	0.0005	350	106	254	10	244	3
ZSZ-1-8	77	370	520	0.71	0.0527	0.0020	0.2858	0.0110	0.0393	0.0004	317	119	255	9	249	3
ZSZ-1-9	98	515	505	1.02	0.0515	0.0017	0.2807	0.0096	0.0395	0.0004	265	78	251	8	250	3
ZSZ-1-10	68	380	262	1.45	0.0549	0.0031	0.2955	0.0156	0.0394	0.0006	406	126	263	12	249	4
ZSZ-1-11	28.6	166	129	1.28	0.0559	0.0046	0.2850	0.0237	0.0371	0.0009	456	185	255	19	235	5
ZSZ-1-12	101	494	528	0.93	0.0570	0.0021	0.3119	0.0113	0.0398	0.0005	500	80	276	9	251	3
ZSZ-1-13	38.4	202	199	1.01	0.0530	0.0029	0.2786	0.0147	0.0387	0.0006	328	126	250	12	245	4
ZSZ-1-14	116	635	465	1.37	0.0505	0.0017	0.2740	0.0093	0.0394	0.0005	217	47	246	7	249	3
ZSZ-1-15	26.1	135	125	1.09	0.0603	0.0034	0.3072	0.0153	0.0385	0.0007	613	122	272	12	243	5
ZSZ-1-16	104	535	628	0.85	0.0497	0.0017	0.2663	0.0093	0.0389	0.0004	189	81	240	7	246	3
ZSZ-1-17	57.9	284	311	0.91	0.0561	0.0026	0.3026	0.0132	0.0396	0.0005	454	102	268	10	251	3
ZSZ-2-1	57.1	279	382	0.73	0.0508	0.0019	0.2711	0.0102	0.0389	0.0005	232	87	244	8	246	3
ZSZ-2-2	41.7	206	282	0.73	0.0555	0.0023	0.3060	0.0129	0.0401	0.0005	432	90	271	10	253	3
ZSZ-2-3	33.0	170	167	1.01	0.0554	0.0028	0.2982	0.0154	0.0391	0.0006	428	115	265	12	247	4
ZSZ-2-4	27.4	133	193	0.69	0.0535	0.0034	0.2811	0.0159	0.0391	0.0006	350	138	252	13	248	4
ZSZ-2-5	37.7	177	287	0.62	0.0511	0.0023	0.2782	0.0126	0.0398	0.0005	243	73	249	10	252	3
ZSZ-2-6	163	933	428	2.18	0.0534	0.0019	0.2827	0.0101	0.0384	0.0005	346	86	253	8	243	3

Table 1. *Cont.*

					Isotopic Ratios						Ages (Ma)					
	($\omega_B/10^{-6}$)				$^{207}Pb/^{206}Pb$		$^{207}Pb/^{235}U$		$^{206}Pb/^{238}U$		$^{207}Pb/^{206}Pb$		$^{207}Pb/^{235}U$		$^{206}Pb/^{238}U$	
Sample No.	**Pb**	**Th**	**U**	**Th/U**	**Ratios**	**1σ**	**Ratios**	**1σ**	**Ratios**	**1σ**	**Ratios**	**1σ**	**Ratios**	**1σ**	**Ratios**	**1σ**
ZSZ-2-7	38.5	193	270	0.71	0.0497	0.0025	0.2614	0.0121	0.0386	0.0006	183	117	236	10	244	4
ZSZ-2-8	42.4	222	207	1.07	0.0590	0.0033	0.3052	0.0162	0.0384	0.0006	566	122	270	13	243	4
ZSZ-2-9	69	352	363	0.97	0.0506	0.0020	0.2753	0.0113	0.0391	0.0006	233	89	247	9	247	4
ZSZ-2-10	35.8	204	147	1.39	0.0559	0.0033	0.2902	0.0172	0.0383	0.0007	450	127	259	14	243	4
ZSZ-2-11	96	506	280	1.81	0.0566	0.0024	0.3088	0.0136	0.0393	0.0005	476	90	273	11	248	3
ZSZ-2-12	55.7	281	243	1.16	0.0594	0.0097	0.3214	0.0514	0.0394	0.0005	583	359	283	39	249	3
ZSZ-2-13	53.2	277	184	1.50	0.0569	0.0030	0.2945	0.0138	0.0389	0.0006	487	115	262	11	246	4
ZSZ-2-14	82	434	401	1.08	0.0541	0.0023	0.2845	0.0112	0.0386	0.0006	376	99	254	9	244	3
ZSZ-2-15	76	355	397	0.90	0.0513	0.0020	0.2926	0.0113	0.0415	0.0005	254	89	261	9	262	3
ZSZ-2-16	85	421	433	0.97	0.0536	0.0023	0.2855	0.0105	0.0390	0.0005	354	101	255	8	247	3
ZSZ-3-1	32.2	91.5	107	0.86	0.0631	0.0032	0.4966	0.0241	0.0578	0.0008	709	107	409	16	362	5
ZSZ-3-2	39.7	104	169	0.61	0.0562	0.0029	0.4451	0.0224	0.0580	0.0008	461	115	374	16	364	5
ZSZ-3-3	51.7	144	195	0.74	0.0604	0.0027	0.4663	0.0185	0.0569	0.0007	620	101	389	13	357	4
ZSZ-3-4	49.0	134	157	0.85	0.0537	0.0025	0.4298	0.0203	0.0580	0.0007	367	103	363	14	363	4
ZSZ-3-5	64.6	173	267	0.65	0.0519	0.0019	0.4201	0.0152	0.0590	0.0007	280	87	356	11	369	4
ZSZ-3-6	98	219	706	0.31	0.0552	0.0015	0.4455	0.0114	0.0585	0.0006	420	56	374	8	367	4
ZSZ-3-7	39.6	129	165	0.78	0.0599	0.0027	0.4744	0.0219	0.0575	0.0008	611	100	394	15	361	5
ZSZ-3-8	27.3	92.0	116	0.80	0.0582	0.0028	0.4596	0.0225	0.0578	0.0009	539	107	384	16	362	5
ZSZ-3-9	40.8	120	207	0.58	0.0593	0.0027	0.4730	0.0217	0.0590	0.0009	576	100	393	15	369	5
ZSZ-3-10	53.8	167	291	0.57	0.0543	0.0021	0.4322	0.0160	0.0584	0.0008	389	89	365	11	366	5

Sixteen zircon grains from the quartz monzonite (ZSZ-2) range from 80 to 160 μm in length, with aspect ratios of 1:1 to 3:1. Most grains exhibit well-defined igneous oscillatory zoning (Figure 4C). The zircon grains have Th and U contents of 133–933 ppm and 147–433 ppm (Table 1), respectively, with Th/U ratios of 0.62–2.18. Sixteen spot analyses yielded $^{206}Pb/^{238}U$ ages ranging from 243 ± 4 Ma to 262 ± 3 Ma (Figure 4C), yielding a weighted mean age of 248 ± 3 Ma (MSWD = 2.1; Figure 4D). This is interpreted as the crystallization age of the quartz monzonite.

Ten zircon grains from the granite dike (ZSZ-3) range from 70 to 150 μm in length, with aspect ratios of 1:1 to 3:1. Most grains exhibit well-defined igneous oscillatory zoning (Figure 4E). The zircon grains have Th and U contents of 91.5–219 ppm and 107–706 ppm, respectively, with Th/U ratios of 0.31–0.86 (Table 1). Ten spot analyses yielded $^{206}Pb/^{238}U$ ages ranging from 357 ± 4 Ma to 369 ± 4 Ma (Figure 4E), yielding a weighted mean age of 364 ± 3 Ma (MSWD = 0.79; Figure 4F). This is interpreted as the crystallization age of the granite dikes.

4.2. Whole-Rock Geochemistry

The major and trace element compositions of the four granite porphyry samples, three quartz monzonite samples, and three granite dike samples are listed in Table 2 and shown in Figure 5.

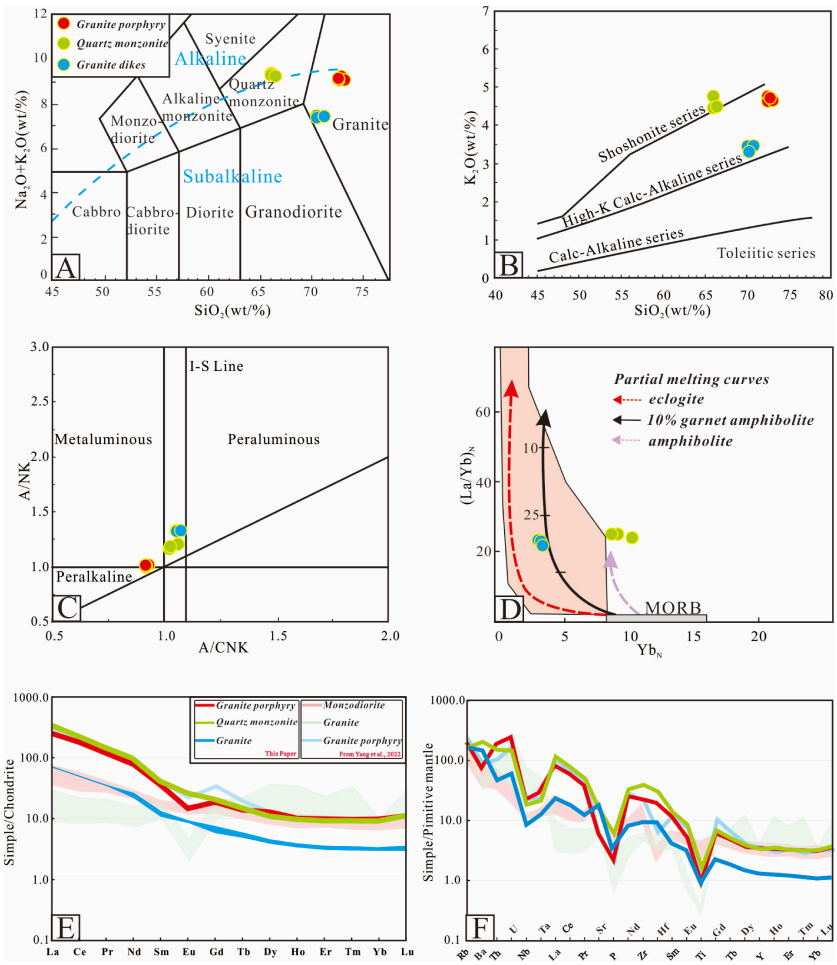


Figure 5. (**A**) Total alkali ($Na_2O + K_2O$) vs. SiO_2 (TAS) diagram [41]. (**B**) K_2O vs. SiO_2 diagram [42]. (**C**) A/CNK vs. A/NK diagram [43], where A = Al_2O_3, C = CaO, N = Na_2O, K = K_2O (all in molar proportions). (**D**) $(La/Yb)_N$ vs. Yb_N diagram for the Zhuanshanzi intrusions [44]. (**E**) Chondrite-normalized REE patterns. (**F**) Primitive mantle-normalized trace element patterns for the Zhuanshanzi intrusions. Chondrite normalizing values are from [45]; primitive mantle values are from [46].

Table 2. Major element (wt.%) and trace element (ppm) data for the granite porphyry (ZSZ1–4), quartz monzonite (ZSZ5–7), and granite dike (ZSZ8–10) samples from the Zhuanshanzi deposit.

Sample No.	ZSZ-1	ZSZ-2	ZSZ-3	ZSZ-4	ZSZ-5	ZSZ-6	ZSZ-7	ZSZ-8	ZSZ-9	ZSZ-10
Rock Type	**Granite Porphyry**				**Quartz Monzonite**			**Granite Dike**		
Age	**245 ± 3 Ma**				**248 ± 3 Ma**			**364 ± 3 Ma**		
SiO_2	72.77	73.08	72.51	72.49	66.02	66.04	66.43	70.08	70.81	70.07
TiO_2	0.23	0.21	0.22	0.22	0.41	0.40	0.40	0.19	0.19	0.19
Al_2O_3	13.67	13.40	13.38	13.72	16.55	16.04	16.10	14.48	14.43	14.52
TFe_2O_3	1.56	1.47	1.60	1.58	2.96	3.04	2.89	1.81	1.83	1.81
MnO	0.05	0.05	0.05	0.05	0.03	0.03	0.03	0.07	0.06	0.05
MgO	0.26	0.25	0.23	0.27	0.60	0.66	0.65	0.49	0.49	0.46
CaO	0.92	0.87	0.85	0.93	1.44	1.47	1.59	2.14	1.89	2.15
Na_2O	4.46	4.37	4.39	4.33	4.45	4.82	4.67	3.91	3.92	4.05
K_2O	4.71	4.64	4.62	4.75	4.76	4.46	4.49	3.45	3.46	3.35
P_2O_5	0.04	0.05	0.04	0.05	0.13	0.13	0.13	0.07	0.07	0.07
LOI	1.49	1.25	1.34	1.30	1.78	1.54	1.65	2.89	2.56	2.84
Total	98.67	98.39	97.89	98.39	97.35	97.09	97.38	96.69	97.15	96.72
A/CNK	0.92	0.92	0.92	0.93	1.06	1.02	1.02	1.05	1.07	1.05
Na_2O/K_2O	0.95	0.94	0.95	0.91	0.93	1.08	1.04	1.13	1.13	1.21
Mg#	0.25	0.25	0.22	0.25	0.29	0.30	0.31	0.35	0.35	0.33
Ti	1330.00	1310.00	1310.00	1290.00	2280.00	2240.00	2150.00	1120.00	1120.00	1130.00
Rb	134.5	126.0	132.0	134.5	119.0	102.5	104.5	113.0	113.0	103.5
Sr	131.5	114.5	127.5	134.5	310	313	333	413	398	383
Y	17.4	16.1	16.3	16.2	16.8	14.5	15.7	6.3	6.3	5.7
Zr	268	236	250	264	498	420	465	123	124	107
Nb	17.7	16.6	17.2	16.6	14.6	13.2	13.5	6.7	6.6	5.7
V	15	10	17	17	48	42	47	35	36	23
Cr	16	23	17	16	9	9	8	12	12	14
Ni	1.3	1.0	0.8	0.6	1.2	1.2	1.2	4.2	4.2	4.8
Ga	17.45	17.70	17.30	18.00	20.2	19.75	19.30	19.15	19.30	20.5
Cs	1.83	1.86	1.94	1.18	4.53	1.86	2.26	10.70	10.80	9.47
Ba	550	510	535	545	1590	1420	1475	1205	1190	977
La	61.5	56.0	58.6	59.3	83.7	74.7	79.1	17.6	17.3	16.9
Ce	112.0	104.0	109.0	110.0	151.0	135.5	142.5	32.1	31.4	30.8
Pr	11.45	10.40	11.10	11.20	15.20	13.60	14.30	3.43	3.37	3.25
Nd	37.5	33.9	35.8	36.4	50.4	44.8	46.8	12.0	11.8	10.9
Sm	5.55	5.13	5.41	5.41	6.81	6.04	6.38	2.00	1.90	1.75
Eu	0.90	0.82	0.85	0.92	1.59	1.42	1.50	0.54	0.53	0.51

Table 2. *Cont.*

Sample No.	ZSZ-1	ZSZ-2	ZSZ-3	ZSZ-4	ZSZ-5	ZSZ-6	ZSZ-7	ZSZ-8	ZSZ-9	ZSZ-10
Rock Type		**Granite Porphyry**				**Quartz Monzonite**			**Granite Dike**	
Age		**245 ± 3 Ma**				**248 ± 3 Ma**			**364 ± 3 Ma**	
Gd	4.05	3.62	3.80	3.83	4.55	3.94	4.21	1.58	1.50	1.28
Tb	0.58	0.53	0.55	0.55	0.62	0.54	0.58	0.21	0.22	0.19
Dy	3.26	2.80	2.97	2.92	3.18	2.73	2.95	1.14	1.14	1.04
Ho	0.63	0.58	0.58	0.57	0.61	0.54	0.58	0.22	0.22	0.20
Er	1.74	1.57	1.63	1.61	1.74	1.50	1.60	0.59	0.57	0.55
Tm	0.27	0.24	0.25	0.25	0.26	0.22	0.24	0.08	0.09	0.08
Yb	1.75	1.62	1.66	1.67	1.78	1.53	1.62	0.55	0.57	0.52
Lu	0.30	0.27	0.28	0.28	0.29	0.27	0.28	0.09	0.09	0.08
Hf	6.9	6.0	6.3	6.3	10.4	8.8	9.8	3.1	3.1	2.8
Ta	1.32	1.36	1.31	1.22	0.88	0.91	0.87	0.49	0.49	0.52
Th	18.00	16.40	16.95	16.65	14.50	13.95	13.50	3.84	3.82	3.87
U	4.48	4.07	4.31	5.30	3.38	3.23	3.12	1.28	1.30	1.21
δEu	0.81	0.81	0.81	0.83	0.96	0.96	0.96	0.97	0.98	1.03
ΣLREE/ΣHREE	23.08	23.71	23.84	24.19	30.12	31.12	30.65	19.12	19.00	20.56
$(La/Yb)_N$	25.21	24.80	25.32	25.47	33.73	35.02	35.02	22.95	21.77	23.31

4.2.1. Granite Porphyry

The granite porphyry samples are characterized by high SiO_2 (72.49–73.08 wt.%) and low Cr (16–23 ppm), Ni (0.6–1.3 ppm), and Mg# (22–25; average 24) values. They have Al_2O_3 contents of 13.38–13.72 wt.%, K_2O contents of 4.62–4.75 wt.%, and Na_2O contents of 4.33–4.46 wt.%, with Na_2O/K_2O ratios of 0.91–0.95. On the total alkali versus silica (TAS) diagram, most samples plot in the subalkaline granite field (Figure 5A), and on the K_2O versus SiO_2 diagram they belong to the high-K calc-alkaline series (Figure 5B). All samples are metaluminous, with aluminum saturation index (ASI = molar $Al_2O_3/(CaO + Na_2O + K_2O)$) values of 0.92–0.93 (Figure 5C).

The total REE concentrations of the granite porphyry samples range from 221.48 to 234.91 ppm. The chondrite-normalized REE patterns (Figure 5E) display pronounced enrichment of light rare-earth elements (LREEs) relative to heavy rare-earth elements (HREEs), with $(La/Yb)_N$ values of 24.80–25.47. All samples exhibit weak negative Eu anomalies (Eu/Eu = 0.81–0.83; average 0.82). On the primitive mantle-normalized multi-element diagram (Figure 5F), all samples are enriched in large-ion lithophile elements (LILEs; e.g., Rb, Ba, K, and Sr) and depleted in high field strength elements (HFSEs; e.g., Ta, Nb, and Ti).

4.2.2. Quartz Monzonite

The quartz monzonite samples have SiO_2 contents of 66.02–66.43 wt.%, and relatively low Cr (8–9 ppm), Ni (~1.2 ppm), and Mg# (29–31; average 30) values. They have Al_2O_3 contents of 16.04–16.55 wt.% and are alkali-rich, with K_2O contents of 4.46–4.76 wt.% and Na_2O contents of 4.45–4.82 wt.% (Na_2O/K_2O = 0.93–1.08). All samples are classified as alkaline quartz monzonite (Figure 5A), belong to the high-K calc-alkaline to shoshonitic series (Figure 5B), and are peraluminous (Figure 5C).

The total REE concentrations of the quartz monzonite samples range from 287.33 to 321.73 ppm. The samples exhibit uniform, strongly fractionated REE patterns (Figure 5E), with pronounced enrichment of LREEs relative to HREEs ($(La/Yb)_N$ = 33.73–35.02) and weak negative Eu anomalies (Eu/Eu* = 0.96). On the primitive mantle-normalized multi-element diagram (Figure 5F), the samples are characterized by weak enrichment in LILEs (e.g., Rb, Ba, K, Sr) and depletion in HFSEs (e.g., Ta, Nb, Ti).

4.2.3. Granite Dikes

The granite dike samples have SiO_2 contents of 70.07–70.81 wt.% and Al_2O_3 contents of 14.43–14.52 wt.%, and relatively low Cr (12–14 ppm), Ni (4.2–4.8 ppm), and Mg# (33–35; average 34) values. The samples are high-K and alkali-rich, with K_2O contents of 3.35–3.46 wt.% and Na_2O contents of 3.91–4.05 wt.% (Na_2O/K_2O = 1.13–1.21). On the total alkali versus silica (TAS) diagram, most samples plot in the subalkaline granite field (Figure 5A), and on the K_2O versus SiO_2 diagram they belong to the high-K calc-alkaline series (Figure 5B). All samples are peraluminous, with ASI values of 1.05–1.07 (Figure 5C).

The total REE concentrations of the samples range from 68.05 to 72.13 ppm. The chondrite-normalized REE patterns (Figure 5E) display pronounced enrichment of LREEs relative to HREEs, with $(La/Yb)_N$ values of 21.77–23.31. All samples show subtle Eu anomalies (Eu/Eu* = 0.97–1.03; average 0.99). On the primitive mantle-normalized multi-element diagram (Figure 5F), the samples are enriched in LILEs (e.g., Rb, Ba, K, Sr) and Zr, and exhibit pronounced negative Nb–Ta and Ti anomalies. The granite dikes have an adakitic affinity (Figure 5D) [44]; with low Y (5.7–6.3 ppm) and Yb (0.52–0.57 ppm); and high Sr (383–413 ppm), Sr/Y (63.17–67.19), and $(La/Yb)_N$ (21.77–23.31).

5. Discussion

5.1. Ages of the Zhuanshanzi Intrusions

The zircon U–Pb dating of the Zhuanshanzi granite porphyry, quartz monzonite, and granite dikes yielded ages of 245 ± 3 Ma, 248 ± 3 Ma, and 364 ± 3 Ma (Figure 4), respectively, revealing two distinct intrusive phases in the Early–Middle Triassic and the Late Devonian.

Numerous Late Paleozoic to Early Mesozoic magmatic rocks are distributed between the central segment of the northern margin of the North China Craton, representing the Late Paleozoic–Early Mesozoic arc magmatism [27,47,48]. Multiple magmatic rocks have been identified in the Zhuanshanzi mining area, including Early Carboniferous monzodiorite, Late Permian granodiorite porphyry [27], and Early Triassic granite [49]; however, Devonian magmatic rocks have not been previously documented. In the context of regional tectonics and magmatic emplacement, these intrusions were generated during the subduction and closure of the Paleo-Asian Ocean beneath the northern margin of the North China Craton. The discovery of Devonian granites thus provides significant constraints on the regional tectonic evolution.

5.2. Petrogenesis of the Zhuanshanzi Intrusions

Granitic diversity arises from variations in tectonic setting, formation environment, source complexity, and magmatic evolution. The Zhuanshanzi intrusions examined here comprise two distinct magmatic stages: the Late Devonian and the Early–Middle Triassic. The petrographic observations confirm that all analyzed samples were fresh, rare secondary phases, with relatively low-to-moderate loss-on-ignition values (LOI = 1.25–2.84 wt.%; Table 2). These features demonstrate that the whole-rock geochemical data retain primary magmatic signatures and are thus suitable for the following petrogenetic discussion. Investigating the petrogenesis of these temporally distinct intrusions provides critical insights into the regional tectonic evolution.

5.2.1. Early–Middle Triassic Zhuanshanzi Intrusions

Middle Triassic Granite Porphyry

The Zhuanshanzi granite porphyry (~245 Ma) is characterized by high SiO_2, relatively low Al_2O_3, high total alkalis ($K_2O + Na_2O \approx 9$ wt.%), and low CaO, and belongs to the high-K calc-alkaline series with metaluminous compositions (Figure 5A–C). Geochemically, the rocks are characterized by depletion in Ba, Nb, P, Eu, and Ti, accompanied by a positive Sr anomaly. These features, together with their high 10,000 × Ga/Al ratios (2.4–2.5), low total REE contents, negative Eu anomalies (Eu/Eu* = 0.81–0.83), and right-sloping REE patterns, are collectively consistent with an A-type granite affinity (Figures 5C,E,F and 6A,B) [50]. These geochemical features are similar to those of the regional Late Permian granite porphyry (253 ± 3 Ma and 252 ± 2 Ma; Figure 5E,F) [27]. Most A-type granites are considered to result from partial melting of the crust during episodes of extension and thinning, and are commonly subdivided into A_1 (anorogenic) and A_2 (post-orogenic) subtypes [50,51]. On the Y–Ce–Nb discrimination diagram, the majority of the Zhuanshanzi granite porphyry samples plot in the A-type granite field and cluster close to the A_1 field, suggesting an affinity with ocean island basalts (OIBs) and emplacement in an intracontinental rift or mantle plume setting (Figure 6C). A-type granites may be generated by several mechanisms: (1) mixing between crustal and mantle-derived melts [52–54]; (2) fractional crystallization of tholeiitic or alkaline basaltic magmas accompanied by crustal assimilation [55,56]; and (3) partial melting of various crustal protoliths triggered by the underplating of mafic magmas [57–59]. The Zhuanshanzi granite porphyry is unlikely to have been generated by fractional crystallization of mantle-derived magmas or by assimilation–mixing processes,

as the rocks lack mafic microgranular enclaves indicative of magma mixing. Moreover, A-type granites generated by fractional crystallization of mantle-derived magmas typically occur as part of a bimodal magmatic suite associated with coeval mafic–ultramafic intrusions [60,61]; however, no such coeval large-scale mafic–ultramafic rocks have been identified in the region. The granite porphyry samples are characterized by low Sr/Y ratios (7.11–8.30), low Yb (1.62–1.75 ppm) and Sr (114.50–134.50 ppm) contents, negative Eu anomalies (δEu = 0.81–0.83), and Ba depletion. The coexistence of negative Eu anomalies and a positive Sr anomaly in the granite porphyry can be explained by breakdown of Sr-rich accessory phases (e.g., apatite, titanite) during partial melting, which released Sr without affecting Eu [62]. The negative Eu anomalies reflect residual plagioclase or limited plagioclase fractionation, while strong Ba depletion indicates K-feldspar control. Although low Yb and Y contents are conventionally attributed to residual garnet in a deep source, the low Sr/Y ratios, negative Eu anomalies, and low Sr concentrations argue against a garnet-dominated, plagioclase-free residuum. Instead, these features are more consistent with plagioclase being a stable residual phase in the source while garnet was absent, implying magma generation at low pressure under amphibolite-facies conditions [62,63]. The low Yb and Y abundances may thus reflect a depleted heavy rare-earth element budget of the source rocks or fractionation of minor amphibole rather than the presence of residual garnet [44,64]. This interpretation is further supported by the zircon Hf isotopic data from the regional Late Permian granite porphyry, which yielded $\varepsilon_{Hf}(t)$ values ranging from −2.58 to +5.50, with corresponding T_{DM2} ages of 1210–1938 Ma [27]. The predominantly negative to weakly positive $\varepsilon_{Hf}(t)$ values, together with the Paleoproterozoic model ages, indicate that the magma was derived mainly from ancient crustal sources. The small positive $\varepsilon_{Hf}(t)$ values suggest limited involvement of juvenile mantle-derived melts or reworking of relatively young crustal materials, but the overall isotopic signature confirms that old crustal components dominated the source [65,66]. This is consistent with the partial melting of a Paleoproterozoic lower crust under low-pressure conditions, as inferred from the whole-rock geochemistry [27]. Following the Late Permian–Early Triassic collisional orogeny between the Xing'an–Mongolian Orogenic Belt and the North China Craton, the study area evolved into a post-orogenic extensional regime [67,68]. This extensional setting likely transitioned progressively into an intracontinental rift environment in the Middle Triassic, possibly triggered by slab break-off or lithospheric delamination, which would have induced asthenospheric upwelling and facilitated crustal partial melting. Such a transition is consistent with the A_1-type affinity of the Zhuanshanzi granite porphyry, which is typically associated with rift- or plume-related anorogenic magmatism. Taken together, the geochemical data indicate that the Triassic granite porphyry was generated by partial melting of ancient crustal material under low-pressure conditions during the post-orogenic to intracontinental rift transition.

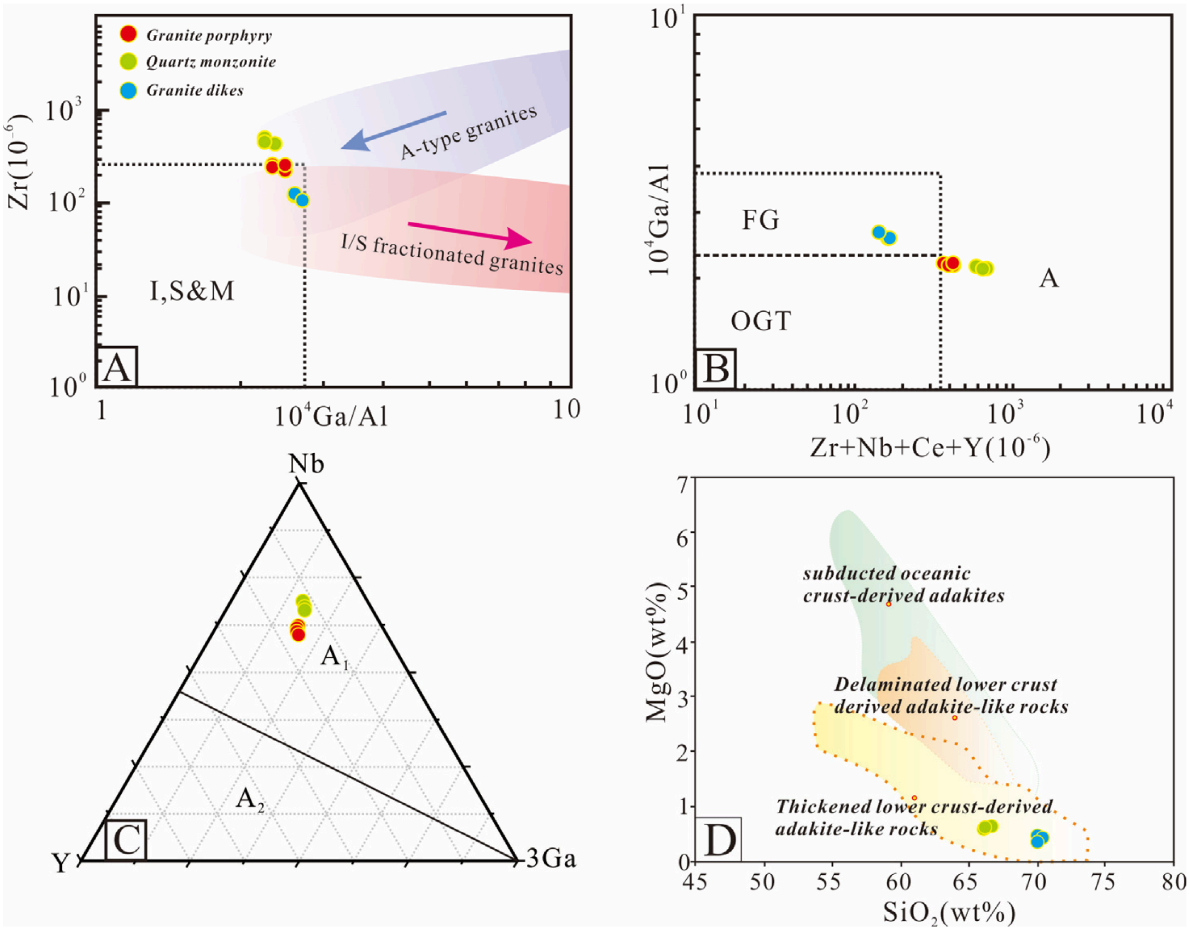


Figure 6. (**A**) 10,000 × Ga/Al vs. Zr diagram. (**B**) Zr + Nb + Ce + Y vs. 10,000 × Ga/Al diagram. A = A-type granites, FG = fractionated felsic granites, OGT = orogenic (I- and S-type) granites. (**C**) Y–Ce–Nb discrimination diagram. (**D**) MgO vs. SiO_2 discrimination diagram for adakitic rocks from the Zhuanshanzi intrusions. (**A**,**B**) after [69]; (**C**) after [70]; (**D**) modified after [71].

Early Triassic Quartz Monzonite

In contrast, the Zhuanshanzi quartz monzonite (~248 Ma) is characterized by high SiO_2 and Al_2O_3, enrichment in alkalis, and low MgO (Figure 5A–C). It displays moderately elevated Sr/Y ratios (18.45–21.59), low Y (14.5–16.5 ppm) and Yb (1.53–1.78 ppm), high $(La/Yb)_N$ (33.73–35.02), and negligible negative Eu anomalies (Eu/Eu* = 0.96). Although the Sr/Y ratios are below the classical adakite threshold (>40), the combination of low Y and Yb and high $(La/Yb)_N$ supports classification as C-type (low-Mg) adakitic granite, which is typically generated by partial melting of a thickened lower crust (Figure 5D) [72,73]. The high $(La/Yb)_N$ and low Yb indicate a garnet-bearing residual assemblage, whereas the slightly negative but near-unity Eu anomaly (≈0.96) and high Sr contents imply that plagioclase was either unstable in the source or that its fractionation was negligible. These features are consistent with melting at pressures > 1.2 GPa and a crustal thickness > 45 km [44,74,75]. However, these pressure estimates are derived from geochemical proxies (e.g., Sr/Y and $(La/Yb)_N$) rather than direct experimental petrological constraints, and therefore carry inherent uncertainties; they should be regarded as approximate indicators of source depth. Notably, this contrasts with the Middle Triassic granite porphyry, whose low Yb is attributed to a depleted HREE budget of the source rather than garnet retention, as supported by its low Sr/Y and pronounced negative Eu anomalies. The distinct residual assemblages of the two Triassic intrusions thus record a progressive change from a thickened, garnet-stable lower crust during the Early Triassic to a thinned, plagioclase-stable crust during the Middle

Triassic [63,76]. On the primitive mantle-normalized multi-element diagram (Figure 5F), the rocks exhibit enrichment in LILEs (e.g., Rb, Ba, K, Sr), Th, U, Y, and Ti, together with pronounced negative Nb–Ta anomalies, attributed to a mantle wedge metasomatized by subduction fluids or to the involvement of arc-type lower crustal sources. Three principal mechanisms have been proposed for the genesis of C-type adakites: (1) high-pressure fractional crystallization of mafic magmas [77,78]; (2) partial melting triggered by delamination of the lower crust [79,80]; and (3) partial melting of a thickened lower crust [67]. The quartz monzonite lacks mafic microgranular enclaves and has uniformly low MgO (0.60–0.66 wt.%), Cr (8–9 ppm), and Ni (1.2 ppm), arguing against significant crust–mantle interaction or magma mixing, and thus excluding high-pressure fractional crystallization. Furthermore, the quartz monzonite shows no evidence of amphibole-dominated fractionation (e.g., decreasing Dy/Yb with increasing SiO_2), and its low MgO, Cr, Ni, and Mg# (29–31) preclude a sanukitoid affinity [81,82]. The delamination model predicts that adakitic melts would have interacted with mantle peridotite during ascent, resulting in elevated MgO, Cr, and Ni [64], and would have been accompanied by coeval mantle-derived mafic magmas and rapid crustal uplift. Such features are absent in the study area during the Late Permian, effectively ruling out a delamination origin. In contrast, partial melting of a thickened lower crust under garnet-stable, plagioclase-absent conditions can explain all the observed geochemical characteristics, including high $(La/Yb)_N$, moderate Sr/Y, low Y–Yb, the near-unity Eu anomaly, and low Mg–Cr–Ni contents (Figure 6D). This interpretation fits the regional tectonic framework, in which the final closure of the Paleo-Asian Ocean led to substantial crustal thickening along the northern margin of the North China Craton [67,68,83–85]. During the waning stage of subduction, the thickened mafic lower crust underwent partial melting, producing C-type adakitic magmas that crystallized to form the Zhuanshanzi quartz monzonite. This magmatic pulse occurred prior to the emplacement of the Middle Triassic A_1-type granite porphyry and therefore records the transition from a compressional to an extensional regime in the region.

The Early Triassic quartz monzonite (~248 Ma) exhibits C-type adakitic affinities, characterized by high Sr/Y ratios, elevated $(La/Yb)_N$, low Yb and Y, and subtle Eu anomalies, together indicating a garnet-bearing, plagioclase-poor residual assemblage consistent with partial melting of a thickened lower crust at pressures > 1.2 GPa [44,74]. This adakitic magmatism reflects substantial crustal thickening following the final closure of the Paleo-Asian Ocean. In contrast, the Middle Triassic granite porphyry (~245 Ma) displays A_1-type geochemical affinities, including high 10,000 × Ga/Al ratios, elevated HFSE contents, and pronounced negative Eu anomalies, which are commonly associated with anorogenic magmatism in extensional settings [69,70]. Although the trace element tectonic discrimination diagrams have inherent uncertainties, the A_1-type signature, together with the low Sr/Y ratios, the absence of garnet in the source, and the inferred low-pressure amphibolite-facies melting conditions, collectively favor an extensional regime. This sharp transition from high-pressure adakitic to low-pressure A_1-type magmatism records the tectonic evolution from a thickened crust during the late- to post-collisional stage to a thinned crust during post-orogenic extension and intracontinental rifting. This interpretation is further supported by published whole-rock geochemical proxies for the northern NCC, which suggest a thickened continental crust of approximately 45–55 km during the Early–Middle Triassic [84,85], consistent with the >45 km crustal thickness inferred from the Zhuanshanzi C-type adakitic quartz monzonite. Therefore, the northern NCC likely remained thickened during the Early Triassic before the rapid extensional thinning recorded by the Middle Triassic A_1-type granite porphyry.

5.2.2. Late Devonian Zhuanshanzi Granite Dikes

As noted above, the Zhuanshanzi granite dikes are peraluminous, high-K calc-alkaline, and adakitic. In contrast to the granite porphyry and quartz monzonite, these dikes were emplaced during the Late Devonian (~364 Ma), indicating a distinct tectonic setting. They are enriched in light rare-earth elements (LREEs), with $(La/Yb)_N$ ratios of 21.77–23.31, reflecting strong LREE/HREE fractionation (Figure 5E). Furthermore, they are enriched in large-ion lithophile elements (LILEs; e.g., Rb, Th, U, K, and Ba) and Zr, and show a pronounced negative Ti anomaly, a geochemical signature typical of I-type granites (Figure 5F). No diagnostic S-type minerals (e.g., garnet, muscovite) are observed, whereas amphibole is present. Accordingly, we interpret the Zhuanshanzi granite dikes as I-type granites (Figure 6A,B). As discussed for the Early Triassic quartz monzonite (Section: Middle Triassic Granite Porphyry), adakitic magmas can be generated by slab melting, amphibole–garnet fractionation, or partial melting of thickened/delaminated lower crust. The geochemical characteristics of the Zhuanshanzi granite dikes, such as elevated K_2O (3.35–3.46 wt.%) and K_2O/Na_2O ratios (0.83–0.88), are inconsistent with an origin by either slab melting or amphibole–garnet fractionation [86,87]. Alternatively, adakitic signatures can be produced by amphibole-dominated fractionation from hydrous basaltic magmas [88]. However, the low MgO (0.46–0.49 wt.%), Cr (12–14 ppm), and Ni (4.2–4.8 ppm) contents of the Zhuanshanzi granite dikes, together with the absence of coeval mafic cumulates, argue against significant amphibole fractionation. The delamination model predicts distinctly elevated MgO, Cr, and Ni due to the interaction with mantle peridotite during ascent, yet the granite dikes have uniformly low MgO, Cr, and Ni, ruling out a delamination origin. Therefore, partial melting of thickened lower continental crust is considered the most plausible mechanism (Figure 6D) [85,89,90]. The low Yb and Y contents and high $(La/Yb)_N$ indicate a garnet-bearing residual assemblage, while the high Sr and weak Eu anomalies imply the plagioclase was unstable in the source, consistent with melting of hydrous basaltic protoliths under amphibolite-facies conditions at pressures > 1.2 GPa (Figure 5D) [44,76]. This adakitic magma was emplaced during the Late Devonian (~364 Ma), significantly earlier than the Triassic magmatic events, suggesting that crustal thickening and partial melting may have occurred episodically during the prolonged evolution of the Paleo-Asian Ocean subduction system.

Although in situ zircon Lu–Hf isotopic data are not available for the Zhuanshanzi intrusions in this study, the published Hf isotopic compositions of coeval magmatic rocks in the Zhuanshanzi area [27] provide important constraints on the crustal source nature. For the Late Carboniferous monzodiorite (340–320 Ma), ten zircon spots yield $\varepsilon_{Hf}(t)$ values of −0.37 to +12.54, with T_{DM2} ages of 656–1799 Ma. For the granite sample (age ca. 250–340 Ma), ten spots give $\varepsilon_{Hf}(t)$ values of +0.88 to +5.24 and T_{DM2} ages of 1281–1673 Ma. More importantly, for the granite porphyry (~252 Ma), nineteen zircon spots display $\varepsilon_{Hf}(t)$ values of −2.58 to +5.50 and T_{DM2} ages of 1210–1938 Ma. The predominantly negative to weakly positive $\varepsilon_{Hf}(t)$ values and Paleoproterozoic model ages indicate that the Triassic magmas were derived largely from ancient crustal sources, consistent with the partial melting of a thickened lower crust as proposed for the C-type adakitic quartz monzonite and the A-type granite porphyry. The scattered positive $\varepsilon_{Hf}(t)$ values in the Carboniferous monzodiorite suggest minor involvement of juvenile mantle material, whereas the dominant crustal signature in the Triassic rocks supports a progressive crustal thickening and maturation during the Late Paleozoic to Early Mesozoic evolution of the northern North China Craton. The zircon U–Pb ages of the Zhuanshanzi intrusions (ca. 248–245 Ma) overlap with the gold mineralization age reported for the deposit (ca. 245 Ma) [25,91]. This temporal coincidence suggests that gold mineralization was genetically linked to the Early–Middle Triassic magmatism, which occurred in a post-collisional extensional

setting. The adakitic quartz monzonite and the A-type granite porphyry both could have provided heat, fluids, and possibly metals for the ore-forming system. In contrast, the Late Devonian adakitic dikes (ca. 364 Ma) show no known coeval gold mineralization in the region, implying that the earlier arc-related magmatism was less fertile for gold.

5.3. Tectonic Setting

The large-scale Late Paleozoic magmatic and thermal events along the northern margin of the North China Craton record the collisional orogeny between the Siberian Craton and the North China Craton during the final closure of the Paleo-Asian Ocean [5,6,10]. The Zhuanshanzi deposit is located at the junction of the Xing'an–Mongolian Orogenic Belt and the North China Craton. From the Late Paleozoic to the Early Mesozoic, at least three major magmatic pulses occurred along the northern margin of the North China Craton: the Devonian (400–360 Ma), the Early Carboniferous to Middle Permian (351–260 Ma), and the Late Permian to Triassic (250–200 Ma). These pulses correspond to successive stages of Paleo-Asian Ocean subduction beneath the North China Craton, collisional orogeny, and subsequent post-orogenic extension [4,13,27]. The Zhuanshanzi intrusions record the latter two pulses, with the Late Devonian granite dikes representing an earlier, localized event.

On the Y + Nb versus Rb and Yb versus Ta tectonic discrimination diagrams (Figure 7A,B), the majority of the Late Devonian to Middle Triassic granite samples from Zhuanshanzi plot in the volcanic-arc granite (VAG) field. It should be noted that granitic magma compositions are strongly influenced by the source rock composition, and tectonic discrimination diagrams based on trace elements have inherent limitations [84]. This limitation is particularly relevant for high-silica granites, which commonly inherit trace element signatures from their crustal protoliths rather than from the active tectonic setting. In the case of the Zhuanshanzi intrusions, the VAG affinity may reflect the contribution of arc-derived lower crustal rocks formed during earlier subduction episodes, rather than contemporaneous subduction. This interpretation is supported by the predominantly ancient crustal Hf model ages (T_{DM2} = 1210–1938 Ma) of the regional Late Permian granite porphyry [27], which indicate a pre-existing arc-type crustal source. Therefore, the VAG affinity observed here may partly reflect inheritance from such an arc-type crustal source rather than a direct fingerprint of contemporaneous subduction. We emphasize that trace element discrimination diagrams alone cannot unambiguously establish coeval subduction, and the tectonic setting inference relies on multiple independent constraints, including regional magmatic associations, structural patterns, and geochronology. Nevertheless, several independent lines of evidence support an active continental margin setting during this period. In the study area, calc-alkaline plutons—including hornblende gabbro, diorite, quartz diorite, granodiorite, and granite—crop out in an east–west-trending belt parallel to the northern margin of the North China Craton and were emplaced during the Carboniferous to Early Permian (358–274 Ma). Their mineralogy, petrochemistry, and isotopic signatures are consistent with those of an active continental margin magmatic arc [18,92,93]. Combined with earlier work [18,94–97], the presence of these high-K calc-alkaline intrusions of Early Carboniferous to Early Permian age implies that subduction lasted for at least ~80 Ma and that the Paleo-Asian Ocean had not yet finally closed. Thus, rather than relying solely on tectonic discrimination diagrams, we integrate geochemical data with regional geology, geochronology, and the temporal–spatial distribution of magmatism to infer a prolonged active continental margin setting associated with the subduction of the Paleo-Asian Ocean beneath the North China Craton.

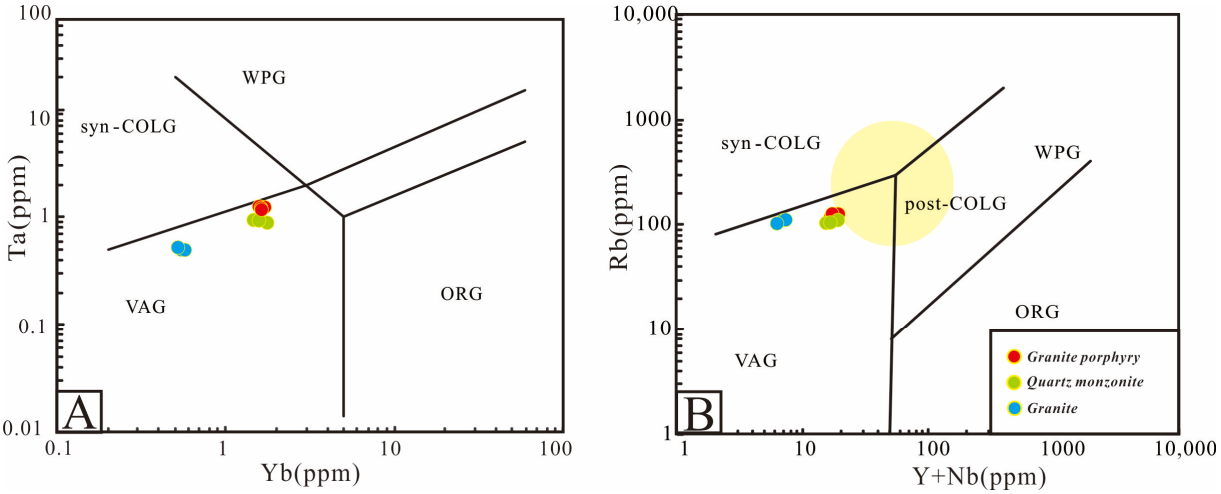


Figure 7. Yb vs. Ta (**A**), Y + Nb vs. Rb (**B**) diagrams for the Zhuanshanzi intrusions [98,99]. Abbreviations: WPG = within-plate granitoids; syn-COLG = syn-collision granitoids; VAG = volcanic-arc granitoids; ORG = ocean-ridge granitoids; post-COLG = post-collision granitoids.

As noted above, the Late Devonian granite dikes at Zhuanshanzi display an adakitic geochemistry and were generated by partial melting of a thickened lower crust. The Early Triassic quartz monzonite is classified as a C-type adakite and was similarly derived from partial melting of a thickened lower crust. The Middle Triassic granite porphyry is an A_1-type granite that was generated by partial melting of crustal material during the transition from post-orogenic extension to intracontinental rifting. Previous studies have shown that the felsic volcanic rocks of the Suji Formation in the Shangdu–Siziwang Banner area display A-type geochemical affinities, pointing to an extensional setting during the Early–Middle Permian, possibly in a back-arc or intra-arc environment. This extensional episode likely represents a precursor stage prior to the onset of collision. Furthermore, a suite of pyroxene diorite, granodiorite, and diorite was emplaced in the Middle Permian (260–269 Ma) [10,30,100]. The geochemical signatures of these Middle Permian intrusions indicate a collisional tectonic setting [30], an interpretation that is further supported by biostratigraphic evidence [49]. In the Early–Middle Triassic, the Paleo-Asian Ocean completed its final closure, marking the culmination of continental collision along the Xilamulun suture. Consequently, it is inferred that collision along the Xilamulun suture between the Xing'an–Mongolian Orogenic Belt and the North China Craton initiated at ca. 270 Ma and terminated at ca. 230 Ma. Previous studies have indicated that from the Late Devonian to the Early Permian, the study area was located in an active continental margin setting, where the Paleo-Asian Ocean subducted beneath the North China Craton. The Late Devonian granite dikes likely formed during arc–arc collisions that led to localized crustal thickening. By the Middle Permian, the study area had evolved into a collisional regime between the Xing'an–Mongolian Orogenic Belt and the North China Craton. During the Late Permian–Early Triassic, the region experienced post-orogenic extension. The quartz monzonite likely crystallized during the late- to post-collisional transition, while the crust remained thickened but underwent intensified deep thermal disturbance. The geochemical signature of the granite porphyry is consistent with a transition from post-orogenic extension to intracontinental rifting following the collisional orogeny. Although a ~3 Myr transition from thickened crust to intracontinental rifting appears rapid, slab break-off or lithospheric delamination can trigger orogenic collapse within a few million years [101,102]. The slab break-off or lithospheric delamination hypothesis is attractive because it can explain the abrupt onset of extensional magmatism and the associated asthenospheric upwelling. The supporting evidence for this includes the A_1-type geochemical signatures

of the Middle Triassic granite porphyry and the presence of coeval high-temperature, low-pressure crustal melting. However, direct geological evidence for slab break-off, such as the presence of syn-break-off mafic magmas or rapid surface uplift, has not been identified in the study area. The available data therefore cannot unambiguously distinguish between slab break-off and lithospheric delamination as the triggering mechanism, and this uncertainty should be kept in mind when interpreting the tectonic transition. Moreover, the Early–Middle Permian A-type volcanic rocks in the region (Section 5.3) indicate that extension was not initiated abruptly in the Middle Triassic but occurred episodically. The ~3 Myr interval should thus be regarded as a minimum estimate, and the actual transition likely spanned a longer period.

5.4. Metallogenic Implications

The spatial and temporal association between granitoid magmatism and gold mineralization at Zhuanshanzi provides important insights into the metallogenic evolution of the northern NCC. The Early Triassic quartz monzonite (ca. 248 Ma) and the Middle Triassic granite porphyry (ca. 245 Ma) are both coeval with the main gold mineralization event (ca. 245 Ma) [91]. In contrast, the Late Devonian granite dikes (ca. 364 Ma) are unrelated to any known coeval gold mineralization in the study area, but they may have provided favorable pre-existing tectonic conditions for subsequent gold mineralization, such as brittle structures and zones of weakness. However, direct geochemical evidence for gold pre-enrichment is lacking. This suggestion therefore remains speculative and requires further verification.

The Triassic intrusions were emplaced during a transitional stage from post-collisional extension to intracontinental rifting, following the final closure of the Paleo-Asian Ocean. Such a tectonic setting is favorable for the generation of high-temperature, hydrous magmas capable of mobilizing and transporting gold [103,104]. The C-type adakitic quartz monzonite, derived from partial melting of thickened lower crust, may have acted as a source of fluids and metals, as adakitic magmas are commonly oxidized and water rich, facilitating the extraction of gold from the lower crust during partial melting [105–107]. The A_1-type granite porphyry, formed by crustal anatexis under high-temperature, low-pressure extensional conditions, indicates an elevated geothermal gradient that would have driven hydrothermal convection and gold precipitation in favorable structural traps, such as the NE–NEE-trending faults that control the distribution of gold orebodies at Zhuanshanzi [91]. The temporal coupling between Triassic magmatism and gold mineralization at Zhuanshanzi (both ca. 245 Ma) suggests a genetic link, where magmatic–hydrothermal fluids exsolved from the crystallizing adakitic and A-type melts may have remobilized gold from the Precambrian basement or from earlier arc-related rocks, and deposited it in extensional structures [108]. This scenario is consistent with the widely accepted model of orogenic gold deposits along craton margins, where post-collisional magmatism provides both the thermal engine and the structural framework for gold mineralization [109,110]. In contrast, the Late Devonian adakitic dikes (ca. 364 Ma) formed during arc–arc collision, a setting that typically generates less voluminous hydrothermal systems and lacks the large-scale extensional structures necessary for significant gold deposition [104]. Although these dikes may have provided favorable pre-existing structural conditions, the absence of synchronous gold mineralization and the lack of direct geochemical fingerprints for gold pre-enrichment indicate that the Devonian arc environment was less fertile for gold, and this inference should be viewed as tentative. The Triassic post-collisional to intracontinental rift transition, by contrast, created optimal conditions for gold mineralization through a combination of crustal extension, elevated heat flow, and the generation of water-rich, oxidized magmas.

6. Conclusions

From the Late Devonian to the Middle Triassic, the Zhuanshanzi area experienced a prolonged tectonic evolution from subduction of the Paleo-Asian Ocean beneath the North China Craton, through arc–continent collision, to post-orogenic extension and intracontinental rifting. The Late Devonian granite dikes (364 ± 3 Ma) formed by partial melting of thickened lower crust during arc–arc collision. The Early Triassic quartz monzonite (248 ± 3 Ma), classified as C-type adakite, originated from partial melting of thickened lower crust during the late- to post-collisional transition. The Middle Triassic granite porphyry (245 ± 3 Ma) displays A_1-type affinities and was generated by crustal melting during the transition from post-orogenic extension to intracontinental rifting. The magmatic pulses in the Zhuanshanzi region thus record the closure of the Paleo-Asian Ocean and the subsequent shift from a compressional to an extensional tectonic regime.

Author Contributions: Formal analysis, X.M., K.S. (Kaituo Shi) and C.W.; investigation, X.M.; writing—original draft, X.M.; writing—review & editing, X.M., K.S. (Kaituo Shi), C.W., K.S. (Kairui Song), H.L. and X.L.; supervision, K.S. (Kaituo Shi); project administration, K.S. (Kaituo Shi); funding acquisition, X.M. and K.S. (Kaituo Shi). All authors have read and agreed to the published version of the manuscript.

Funding: This work is supported by the Inner Mongolia Natural Science Foundation (No. 2025MS04057), the National Natural Science Foundation of China (No. 42502066), the Scientific Research Foun-dation of Hunan Provincial Education Department (No. 24C0212), and the Opening Foundation of Beijing SHRIMP Center (No. DDK24-031).

Data Availability Statement: All data supporting the reported results are included in the manuscript, including the supplementary tables and figures.

Acknowledgments: We gratefully acknowledge the editors and reviewers for their constructive comments and suggestions regarding the manuscript.

Conflicts of Interest: The authors declare that they have no known competing financial interests or personal relationships that could have appeared to influence the work reported in this paper.

References

1. Zhou, T.H.; Goldfarb, R.J.; Phillips, G.N. Tectonics and distribution of gold deposits in China—An overview. *Miner. Depos.* **2002**, *37*, 249–282. [CrossRef]
2. Liu, D.Y.; Nutman, A.P.; Compston, W.; Wu, J.S.; Shen, Q.H. Remnants of 3800 Ma crust in the Chinese part of the North China Craton. *Geology* **1992**, *20*, 329–342. [CrossRef]
3. Zhao, G.C.; Sun, M.; Wilde, S.A.; Li, S.Z. Late Archean to Paleoproterozoic evolution of the North China Craton: Key issues revisited. *Precambrian Res.* **2005**, *136*, 177–202. [CrossRef]
4. Zhao, G.C.; Cawood, P.A.; Li, S.Z.; Wilde, S.A.; Sun, M.; Zhang, J.; He, Y.H.; Yin, C.Q. Amalgamation of the North China Craton: Key issues and discussion. *Precambrian Res.* **2012**, *222–223*, 55–76. [CrossRef]
5. Di, Q.; Xue, G.; Lei, D.; Zeng, Q.; Fu, C.; An, Z. Summary of technology for a comprehensive geophysical exploration of gold mine in North China Craton. *Sci. China Earth Sci.* **2021**, *64*, 1524–1536. [CrossRef]
6. Zhao, Y.; Zhai, M.G.; Chen, H.; Zhang, S.H. Paleozoic–Early Jurassic tectonic evolution of North China Craton and its adjacent orogenic belts. *Geol. China* **2017**, *44*, 44–60. (In Chinese with English Abstract).
7. Wu, F.Y.; Yang, J.H.; Xu, Y.G.; Wilde, S.A.; Walker, R.J. Destruction of the North China Craton in the Mesozoic. *Annu. Rev. Earth Planet. Sci.* **2019**, *47*, 173–195. [CrossRef]
8. Pirajno, F.; Ernst, R.E.; Borisenko, A.S.; Fedoseev, G.; Naumov, E.A. Intraplate magmatism in Central Asia and China and associated metallogeny. *Ore Geol. Rev.* **2009**, *35*, 114–136. [CrossRef]
9. Seltmann, R.; Soloviev, S.; Shatov, V.; Pirajno, F.; Naumov, E.; Cherkasov, S. Metallogeny of Siberia: Tectonic, geologic and metallogenic settings of selected significant deposits. *Aust. J. Earth Sci.* **2010**, *57*, 655–706. [CrossRef]
10. Sun, Z.J. Study on Gold Deposits Mineralization in Chifeng-Chaoyang Margin of North China Craton Region. Ph.D. Dissertation, Jilin University, Changchun, China, 2013. (In Chinese with English Abstract).

11. Fu, L.B.; Wei, J.H.; Chen, H.Y.; Bagas, L.; Tan, J.; Li, H.; Zhang, D.H.; Tian, N. The relationship between gold mineralization, exhumation of metamorphic core complex and magma cooling: Formation of the Anjiayingzi Au deposit, northern North China Craton. *Ore Geol. Rev.* **2016**, *73*, 222–240. [CrossRef]
12. Zhang, L.C.; Bai, Y.; Zhu, M.T.; Huang, K.; Peng, Z.D. Regional heterogeneous temporal–spatial distribution of gold deposits in the North China Craton: A review. *Geol. J.* **2020**, *55*, 5646–5663. [CrossRef]
13. Zeng, Q.D.; Wang, Y.B.; Yang, J.H.; Guo, Y.P.; Yu, B.; Zhou, L.L.; Qiu, H.C. Spatial-temporal distribution and tectonic setting of gold deposits in the Northern margin gold belt of the North China Craton. *Int. Geol. Rev.* **2021**, *63*, 941–972. [CrossRef]
14. Sun, D.Y.; Wu, F.Y.; Zhang, Y.B.; Gao, S. The final closing time of the west Lamulun River–Changchun–Yanji plate suture zone—Evidence from the Dayushan granitic pluton, Jilin Province. *J. Jilin Univ. (Earth Sci. Ed.)* **2004**, *34*, 174–181.
15. Li, J.Y. Permian geodynamic setting of Northeast China and adjacent regions: Closure of the Paleo-Asian Ocean and subduction of the Paleo-Pacific plate. *J. Asian Earth Sci.* **2006**, *26*, 207–224. [CrossRef]
16. Windley, B.F.; Alexeiev, D.; Xiao, W.J.; Kröner, A.; Badarch, G. Tectonic models for accretion of the Central Asian Orogenic Belt. *J. Geol. Soc.* **2007**, *164*, 31–47. [CrossRef]
17. Chen, Y.J.; Li, N. Nature of ore-fluids of intra-continental intrusion-related hypothermal deposits and its difference from those in island arcs. *Acta Petrol. Sin.* **2009**, *25*, 2477–2508. (In Chinese with English Abstract).
18. Zhang, S.H.; Zhao, Y.; Song, B.; Hu, J.M.; Liu, S.W.; Yang, Y.H.; Chen, F.K.; Liu, X.M.; Liu, J. Contrasting Late Carboniferous and Late Permian–Middle Triassic intrusive suites from the northern margin of the North China Craton: Geochronology, petrogenesis and tectonic implications. *Geol. Soc. Am. Bull.* **2009**, *121*, 181–200.
19. Liu, C.H.; Wu, C.L.; Gao, Y.H.; Lei, M.; Qin, H.P.; Li, M.Z. Zircon LA-ICP-MS U–Pb dating and Lu–Hf isotopic system of A-type granitoids in South Tianshan, Baicheng County, Xinjiang. *Acta Petrol. Sin.* **2014**, *30*, 1595–1614. (In Chinese with English Abstract).
20. Yang, F. Metallogenic Study of Epithermal Gold Deposits in Chifeng-Chaoyang Area, the Eastern Section of the Margin of the North China Platform. Ph.D. Dissertation, Jilin University, Changchun, China, 2019. (In Chinese with English Abstract).
21. Shi, K.T.; Wang, K.Y.; Wang, R.; Ma, X.L.; Sun, L.X.; Yang, H. Geological, fluid inclusion, and O–C–S–Pb–He–Ar isotopic constraints on the genesis of the Honghuagou lode gold deposit, northern North China Craton. *Geochemistry* **2021**, *81*, 125807. [CrossRef]
22. Kusky, T.M.; Windley, B.F.; Zhai, M.G. Tectonic evolution of the North China Block: From orogen to craton to orogen. In *Mesozoic Sub-Continental Lithospheric Thinning Under Eastern Asia*; Zhai, M.G., Windley, B.F., Kusky, T.M., Meng, Q.R., Eds.; Geological Society, London, Special Publications: London, UK, 2007; Volume 280, pp. 1–34.
23. Hou, W.R. Contrast Study on the Hadamengou Gold Deposit and Jinchanggouliang Gold Deposit, Inner Mongolia. Master's Thesis, Chinese Academy of Geological Science, Beijing, China, 2011. (In Chinese with English Abstract).
24. Fu, L.B.; Wei, J.H.; Kusky, T.M.; Chen, H.Y.; Tan, J.; Li, Y.J.; Shi, W.J.; Chen, C.; Zhao, S.Q. The Cretaceous Duimiangou adakite-like intrusion from the Chifeng region, northern North China Craton: Crustal contamination of basaltic magma in an intracontinental extensional environment. *Lithos* **2012**, *134–135*, 273–288. [CrossRef]
25. Sun, H.; Li, X.; Wang, F.; Zhang, M. Geochronology and geochemistry of the Zhuanshanzi gold deposit: Implications for Early Triassic gold mineralization in the Chifeng-Chaoyang area. *Ore Geol. Rev.* **2018**, *95*, 118–135.
26. Liu, L.; Gu, X.X.; Zhang, Y.M.; Ouyang, X.; Wang, L.Z.; Gao, L.Y. Genesis of the Jinchanggouliang gold deposit, Chifeng, China: Constraints from fluid inclusions and isotopic geochemistry. *Ore Geol. Rev.* **2019**, *115*, 103180. [CrossRef]
27. Yang, F.; Jiang, Y.Y.; Chen, J.S.; Han, X. Chronology and geochemistry of Carboniferous-Permian intrusive rocks in Zhuanshanzi mining area, Chifeng, middle part of the northern margin of the North China Craton: Constraints on the tectonic evolution of the Paleo-Asian Ocean. *Acta Petrol. Sin.* **2022**, *38*, 2467–2488, (In Chinese with English Abstract). [CrossRef]
28. Xiao, T.T. The Sources of Ore-Forming Materials for Gold Deposits in the Northern Margin of the North China Craton: Constraints from Hg–S Isotopes and Pyrite Trace Elements. Master's Thesis, Jilin University, Changchun, China, 2024. (In Chinese with English abstract).
29. Zhang, S.H.; Zhao, Y.; Liu, J.M.; Hu, Z.C. Different sources involved in generation of continental arc volcanism: The Carboniferous–Permian volcanic rocks in the northern margin of the North China block. *Lithos* **2016**, *240–243*, 382–401. [CrossRef]
30. Chen, J.S. Petrogenesis of the Late Paleozoic to Early Mesozoic Granitic Rocks from the Chifeng Region and Their Tectonic Implication. Ph.D. Dissertation, Jilin University, Changchun, China, 2018. (In Chinese with English Abstract).
31. Ma, G.X. Structure style and evolution features in western district of Chifeng of Chifeng-Kaiyuan Fault. *Glob. Geol.* **2018**, *37*, 791–803, (In Chinese with English Abstract).
32. Yang, Q.; Shi, W.; Hou, G.T.; Zhang, Y.; Wang, T.Y.; Zhao, Z.X. Late Mesozoic intracontinental deformation at the northern margin of the North China Craton: A case study from the Kalaqin massif, southeastern Inner Mongolia, China. *Tectonophysics* **2020**, *793*, 228591. [CrossRef]

33. Zhang, L.D. Geological characteristics and genesis of gold deposits in Jinchanggouliang region. *Bull. Shenyang Inst. Geol. Min. Res. Chin. Acad. Geol. Sci.* **1990**, *21*, 1–13. (In Chinese with English Abstract).
34. Zhang, X.B.; Wang, K.Y.; Fu, L.J.; Zhang, M.; Konare, Y.; Peng, D.W.; Cai, W.Y. Fluid inclusions, C–H–O–S isotope and geochronology of the Bujinhei Pb–Zn deposit in the southern Great Xing'an Range of Northeast China: Implication for ore genesis. *Resour. Geol.* **2017**, *67*, 207–227. [CrossRef]
35. Wiedenbeck, M.; Allé, P.; Corfu, F.; Griffin, W.L.; Meier, M.; Oberli, F.; von Quadt, A.; Roddick, J.C.; Spiegel, W. Three natural zircon standards for U–Th–Pb, Lu–Hf, trace element and REE analyses. *Geostand. Newsl.* **1995**, *19*, 1–23. [CrossRef]
36. Sláma, J.; Košler, J.; Condon, D.J.; Crowley, J.L.; Gerdes, A.; Hanchar, J.M.; Horstwood, M.S.; Morris, G.A.; Nasdala, L.; Norberg, N.; et al. Plešovice zircon—A new natural reference material for U–Pb and Hf isotopic microanalysis. *Chem. Geol.* **2008**, *249*, 1–35. [CrossRef]
37. Ludwig, K.R. *ISOPLOT 3.0: A Geochronological Toolkit for Microsoft Excel*; Berkeley Geochronology Center Special Publication: Berkeley, CA, USA, 2003; p. 70.
38. Andersen, T. Correction of common lead in U–Pb analyses that do not report ^{204}Pb. *Chem. Geol.* **2002**, *192*, 59–79. [CrossRef]
39. Hoskin, P.W.O.; Black, L.P. Metamorphic zircon formation by solid-state recrystallization of protolith igneous zircon. *J. Metamorph. Geol.* **2000**, *18*, 423–439. [CrossRef]
40. Belousova, E.A.; Griffin, W.L.; O'Reilly, S.Y.; Fisher, N.I. Igneous zircon: Trace element composition as an indicator of source rock type. *Contrib. Mineral. Petrol.* **2002**, *143*, 602–622. [CrossRef]
41. Middlemost, E.A. Naming materials in the magma/igneous rock system. *Earth-Sci. Rev.* **1994**, *37*, 215–224. [CrossRef]
42. Peccerillo, A.; Taylor, S.R. Geochemistry of Eocene calc-alkaline volcanic rocks from the Kastamonu area, northern Turkey. *Contrib. Miner. Petrol.* **1976**, *58*, 63–81. [CrossRef]
43. Maniar, P.D.; Piccoli, P.M. Tectonic discrimination of granitoids. *Geol. Soc. Am. Bull.* **1989**, *101*, 635–643. [CrossRef]
44. Defant, M.J.; Drummond, M.S. Derivation of some modern arc magmas by melting of young subducted lithosphere. *Nature* **1990**, *347*, 662–665. [CrossRef]
45. Sun, S.S.; McDonough, W.F. Chemical and isotopic systematics of oceanic basalts: Implications for mantle composition and processes. In *Magmatism in the Ocean Basins*; Saunders, A.D., Norry, M.J., Eds.; Geological Society, London, Special Publications: London, UK, 1989; Volume 42, pp. 313–345.
46. McDonough, W.F.; Sun, S.S. Composition of the Earth. *Chem. Geol.* **1995**, *120*, 223–253. [CrossRef]
47. Shao, J.A.; Zhang, Z.; She, H.Q.; Liu, D.S. The discovery of Phanerozoic granulite in Chifeng area of North China Craton and its implication. *Earth Sci. Front.* **2012**, *19*, 188–198, (In Chinese with English Abstract).
48. Xu, B.W.; Xi, A.H.; Ge, Y.H.; Liu, J.; Wang, M.Z.; Fang, C. Zircon U–Pb ages of the Late Paleozoic A-type granites in Chifeng, Inner Mongolia and its tectonic significance. *Acta Geol. Sin.* **2015**, *89*, 58–69. (In Chinese with English Abstract).
49. Sun, Y.W.; Ding, H.S.; Liu, H.; Zhang, D.J.; Gong, F.H.; Zheng, Y.J. Fossil plants from the Guadalupian Yujiabeigou Formation in the northern margin of North China Plate and their tectonic implications. *J. Jilin Univ. (Earth Sci. Ed.)* **2016**, *46*, 1268–1283. (In Chinese with English Abstract).
50. Zhang, Q. The criteria and discrimination for A-type granites: A reply to the question put forward by Wang Yang and some other persons for "A-type granite: What is the essence?". *Acta Petrol. Mineral.* **2013**, *32*, 267–274. (In Chinese with English Abstract).
51. Jia, X.H.; Wang, Q.; Tang, G.J. A-type granites: Research progress and implications. *Geotect. Metallog.* **2009**, *33*, 465–480. (In Chinese with English Abstract).
52. Kerr, A.; Fryer, B.J. Nd isotope evidence for crust-mantle interaction in the generation of A-type granitoid suites in Labrador, Canada. *Chem. Geol.* **1993**, *104*, 39–60. [CrossRef]
53. Kemp, A.I.S.; Wormald, R.J.; Whitehouse, M.J.; Price, R.C. Hf isotopes in zircon reveal contrasting sources and crystallization histories for alkaline to peralkaline granites of Temora, southeastern Australia. *Geology* **2005**, *33*, 797–800. [CrossRef]
54. Wong, J.; Sun, M.; Xing, G.F.; Li, X.H.; Zhao, G.C.; Wong, K.; Yuan, C.; Xia, X.P.; Li, L.M.; Wu, F.Y. Geochemical and zircon U–Pb and Hf isotopic study of the Baijuhuajian metaluminous A-type granite: Extension at 125–100 Ma and its tectonic significance for South China. *Lithos* **2009**, *112*, 289–305. [CrossRef]
55. Mushkin, A.; Navon, O.; Halicz, L.; Hartmann, G.; Stein, M. The petrogenesis of A-type magmas from the Amram Massif, southern Israel. *J. Petrol.* **2003**, *44*, 815–832. [CrossRef]
56. Bonin, B. A-type granites and related rocks: Evolution of a concept, problems and prospects. *Lithos* **2007**, *97*, 1–29. [CrossRef]
57. Creaser, R.A.; Price, R.C.; Wormald, R.J. A-type granites revisited: Assessment of a residual-source model. *Geology* **1991**, *19*, 163–166. [CrossRef]
58. King, P.L.; White, A.J.R.; Chappell, B.W.; Allen, C.M. Characterization and origin of aluminous A-type granites from the Lachlan Fold Belt, Southeastern Australia. *J. Petrol.* **1997**, *38*, 371–391. [CrossRef]

59. Wu, Q.; Niu, M.L.; Zhu, G.; Wang, T.; Fei, L.L. Zircon U–Pb age, petrogenesis of the Changgang A-type granites in the Lujiang segment of the Tan-Lu fault zone and their implication. *Acta Petrol. Sin.* **2016**, *32*, 1031–1048. (In Chinese with English Abstract).
60. Turner, S.P.; Foden, J.D.; Morrison, R.S. Derivation of some A-type magmas by fractionation of basaltic magma: An example from the Padthaway Ridge, South Australia. *Lithos* **1992**, *28*, 151–179. [CrossRef]
61. Xue, F.H.; Zhang, X.H.; Deng, J.X.; Yuan, L.L. Late Jurassic A-type granite from the Dalai region of central Inner Mongolia: Geochemistry, petrogenesis and tectonic implication. *Acta Petrol. Sin.* **2015**, *31*, 1774–1788. (In Chinese with English Abstract).
62. Patiño Douce, A.E. What do experiments tell us about the relative contributions of crust and mantle to the origin of granitic magmas? In *Understanding Granites: Integrating New and Classical Techniques*; Castro, A., Fernández, C., Vigneresse, J.L., Eds.; Geological Society, London, Special Publications: London, UK, 1999; Volume 168, pp. 55–75.
63. Beard, J.S.; Lofgren, G.E. Dehydration melting and water-saturated melting of basaltic and andesitic greenstones and amphibolites at 1, 3, and 6.9 kbar. *J. Petrol.* **1991**, *32*, 365–401. [CrossRef]
64. Zhang, Q.; Wang, Y.; Li, C.D.; Wang, Y.L.; Jin, W.J.; Jia, X.Q. Granite classification on the basis of Sr and Yb contents and its implications. *Acta Petrol. Sin.* **2006**, *22*, 2249–2269, (In Chinese with English Abstract).
65. Kemp, A.I.S.; Hawkesworth, C.J.; Foster, G.L.; Paterson, B.A.; Woodhead, J.D.; Hergt, J.M.; Gray, C.M.; Whitehouse, M.J. Magmatic and crustal differentiation history of granitic rocks from Hf–O isotopes in zircon. *Science* **2007**, *315*, 980–983. [CrossRef]
66. Yang, J.H.; Wu, F.Y.; Wilde, S.A.; Belousova, E.; Griffin, W.L. Mesozoic decratonization of the North China Block. *Geology* **2008**, *36*, 467–470. [CrossRef]
67. Zhang, Y.J.; Zhang, C.; Ma, Y.F.; Yang, T.; Liu, Y.; Du, J.Y.; Zhao, Y.L.; Zhang, J.K. Closure time of the eastern Paleo-Asian Ocean: Constraint from Permian-Triassic strata and detrital zircon geochronology at southern Great Xing'an Mountains, Inner Mongolia (China). *Acta Petrol. Sin.* **2022**, *38*, 2781–2810. (In Chinese with English Abstract). [CrossRef]
68. Li, S.; Wang, T.; Xiao, W.J.; Hou, Q.L. Tectono-magmatic evolution from accretion to collision in the southern margin of the Central Asian Orogenic Belt. *Acta Petrol. Sin.* **2023**, *39*, 1261–1275. (In Chinese with English Abstract). [CrossRef]
69. Whalen, J.B.; Currie, K.L.; Chappell, B.W. A-type granites: Geochemical characteristics, discrimination and petrogenesis. *Contrib. Mineral. Petrol.* **1987**, *95*, 407–419. [CrossRef]
70. Eby, G.N. Chemical subdivision of the A-type granitoids: Petrogenetic and tectonic implications. *Geology* **1992**, *20*, 641–644. [CrossRef]
71. Wang, D.D.; Li, S.Z.; Zhou, X.G.; Liu, W.W.; Lin, Y.H.; Zeng, Q.N.; Zhang, W.H. SHRIMP U–Pb dating of detrital zircon from the Upper Permian Linxi Formation in eastern Inner Mongolia, and its geological significance. *Geol. Rev.* **2016**, *62*, 1021–1040. (In Chinese with English Abstract).
72. Zhang, Q.; Wang, Y.; Liu, W.; Wang, Y.L. Adakite: Its characteristics and implications. *Geol. Bull. China* **2002**, *21*, 431–435. (In Chinese with English Abstract).
73. Cai, J.H.; Yan, G.H.; Mu, B.L.; Ren, K.X.; Song, B. Zircon U–Pb age, Sr–Nd–Pb isotopic compositions and trace element of Fangshan complex in Beijing and their petrogenesis significance. *Acta Petrol. Sin.* **2005**, *21*, 776–788. (In Chinese with English Abstract).
74. Qian, Q.; Hermann, J. Partial melting of lower crust at 10–15 kbar: Constraints on adakite and TTG formation. *Contrib. Mineral. Petrol.* **2013**, *165*, 1195–1224. [CrossRef]
75. Väisänen, M.; Johansson, Å.; Andersson, U.; Eklund, O.; Hölttä, P. Palaeoproterozoic adakite- and TTG-like magmatism in the Svecofennian orogen, SW Finland. *Geol. Acta* **2012**, *10*, 351–371. [CrossRef]
76. Rapp, R.P.; Xiao, L.; Shimizu, N. Experimental constraints on the origin of potassium-rich adakite in east China. *Acta Petrol. Sin.* **2002**, *18*, 293–302.
77. Chiaradia, M. Adakite-like magmas from fractional crystallization and melting-assimilation of mafic lower crust (Eocene Macuchi arc, Western Cordillera, Ecuador). *Chem. Geol.* **2009**, *265*, 468–487. [CrossRef]
78. Castillo, P.R. Adakite petrogenesis. *Lithos* **2012**, *134*, 304–316. [CrossRef]
79. Kay, R.W.; Kay, S.M. Delamination and delamination magmatism. *Tectonophysics* **1993**, *219*, 177–189. [CrossRef]
80. Wang, F.; Zhou, X.H.; Zhang, L.C.; Ying, J.F.; Zhang, Y.T.; Wu, F.Y.; Zhu, R.X. Late Mesozoic volcanism in the Great Xing'an Range (NE China): Timing and implications for the dynamic setting of NE Asia. *Earth Planet. Sci. Lett.* **2006**, *251*, 179–198. [CrossRef]
81. Heilimo, E.; Halla, J.; Hölttä, P. Discrimination and origin of the sanukitoid series: Geochemical constraints from the Neoarchean western Karelian Province (Finland). *Lithos* **2010**, *115*, 27–39. [CrossRef]
82. Kovalenko, A.V.; Clemens, J.D.; Savatenkov, V.M. Petrogenetic constraints for the genesis of Archaean sanukitoid suites: Geochemistry and isotopic evidence from Karelia, Baltic Shield. *Lithos* **2005**, *79*, 147–160. [CrossRef]
83. Liu, J.F.; Chi, X.G.; Zhao, Z.; Hu, Z.C.; Chen, J.Q. Zircon U–Pb age and petrogenetic discussion on Jianshetun adakite in Balinyouqi, Inner Mongolia. *Acta Petrol. Sin.* **2013**, *29*, 827–839. (In Chinese with English Abstract).

84. Li, S.; Chung, S.L.; Wilde, S.A.; Jahn, B.M.; Xiao, W.J.; Wang, T.; Guo, Q.Q. Early–Middle Triassic high Sr/Y granitoids in the southern Central Asian Orogenic Belt: Implications for ocean closure in accretionary orogens. *J. Geophys. Res. Solid Earth* **2017**, *122*, 2291–2309. [CrossRef]
85. Deng, C.Z.; Sun, G.Y.; Sun, D.Y.; Huang, H.; Zhang, J.F.; Gou, J. Origin of C-type adakite magmas in the NE Xing'an block, NE China and tectonic implication. *Acta Geochim.* **2018**, *37*, 281–294. [CrossRef]
86. Macpherson, C.G.; Dreher, S.T.; Thirlwall, M.F. Adakites without slab melting: High pressure differentiation of island arc magma, Mindanao, the Philippines. *Earth Planet. Sci. Lett.* **2006**, *243*, 581–593. [CrossRef]
87. Kamvong, T.; Zaw, K.; Meffre, S.; Maas, R.; Stein, H.; Lai, C.-K. Adakites in the Truong Son and Loei fold belts, Thailand and Laos: Genesis and implications for geodynamics and metallogeny. *Gondwana Res.* **2014**, *26*, 165–184. [CrossRef]
88. Castillo, P.R.; Janney, P.E.; Solidum, R.U. Petrology and geochemistry of Camiguin Island, southern Philippines: Insights to the source of adakites and other lavas in a complex arc setting. *Contrib. Miner. Petrol.* **1999**, *134*, 33–51. [CrossRef]
89. Wang, Q.; Xu, J.F.; Jian, P.; Bao, J.W.; Zhao, Z.H.; Li, C.F.; Xiong, X.L.; Ma, J.L. Petrogenesis of adakitic porphyries in an extensional tectonic setting, Dexing, South China: Implications for the genesis of porphyry copper mineralization. *J. Petrol.* **2006**, *47*, 119–144. [CrossRef]
90. Golestani, M.; Karimpour, M.H.; Shafaroudi, A.M.; Shahri, M.R.H. Geochemistry, U–Pb geochronology and Sr–Nd isotopes of the Neogene igneous rocks, at the Iju porphyry copper deposit, NW Shahr-e-Babak, Iran. *Ore Geol. Rev.* **2018**, *93*, 290–307. [CrossRef]
91. Sun, Z.J.; Wang, Z.Q.; Yu, H.N.; Wang, C.Y.; Liu, G.H.; Bai, X.D. Fluid inclusions and C–H–O–S–Pb isotopes: Implications for the genesis of the Zhuanshanzi gold deposit on the northern margin of the North China Craton. *Resour. Geol.* **2018**, *69*, 1–21. [CrossRef]
92. Zhang, S.H.; Zhao, Y.; Song, B.; Wu, H. The Late Paleozoic gneissic granodiorite pluton in early Precambrian high-grade metamorphic terrains near Longhua County in northern Hebei Province, North China: Result from zircon SHRIMP U–Pb dating and its tectonic implications. *Acta Petrol. Sin.* **2004**, *20*, 621–626. (In Chinese with English Abstract).
93. Zhang, C.; Liu, S.W.; Han, B.F.; He, G.Q.; Huang, B.L. SHRIMP U–Pb dating of Dashigou biotite–K-feldspar granites in Shangdu, Inner Mongolia, and its significance. *Acta Petrol. Sin.* **2007**, *23*, 591–596. (In Chinese with English Abstract).
94. Wang, H.C.; Zhao, F.Q.; Li, H.M.; Sun, L.X.; Miao, L.C.; Ji, S.P. Zircon SHRIMP U–Pb age of the dioritic rocks from northern Hebei: The geological records of late Paleozoic magmatic arc. *Acta Petrol. Sin.* **2007**, *23*, 597–604. (In Chinese with English Abstract).
95. Wang, W.Q.; Liu, Z.H.; Wang, X.A.; Zhang, C.; Fan, Z.W.; Shi, Y.; Zhu, K. SHRIMP U–Pb dating of the zircon from the Hercynian biotite monzonitic granites in Urad Zhongqi, Inner Mongolia, and its geological significance. *J. Jilin Univ. (Earth Sci. Ed.)* **2012**, *42*, 1771–1782. (In Chinese with English Abstract).
96. Zhang, S.H.; Zhao, Y.; Davis, G.A.; Ye, H.; Wu, F. Temporal and spatial variations of Mesozoic magmatism and deformation in the North China Craton: Implications for lithospheric thinning and decratonization. *Earth-Sci. Rev.* **2014**, *131*, 49–87. [CrossRef]
97. Li, S.; Wilde, S.A.; Wang, T.; Xiao, W.J.; Guo, Q.Q. Latest Early Permian granitic magmatism in southern Inner Mongolia, China: Implications for the tectonic evolution of the southeastern Central Asian Orogenic Belt. *Gondwana Res.* **2016**, *29*, 168–180. [CrossRef]
98. Pearce, J.A. Sources and settings of granitic rocks. *Episodes* **1996**, *19*, 120–125. [CrossRef]
99. Pearce, J.A.; Harris, N.B.W.; Tindle, A.G. Trace element discrimination diagrams for the tectonic interpretation of granite rocks. *J. Petrol.* **1984**, *25*, 956–983. [CrossRef]
100. Xi, A.H.; Ma, Y.J.; Ge, Y.H.; Tang, X.Y.; Liu, S.; Xu, B.W.; Liu, J. Multi-stage intrusive evidence and geological significance of Dayingzi granite in Chifeng, eastern Inner Mongolia. *J. Jilin Univ. (Earth Sci. Ed.)* **2015**, *45*, 791–803. (In Chinese with English Abstract).
101. Davies, J.H.; von Blanckenburg, F. Slab breakoff: A model of lithosphere detachment and its test in the magmatism and deformation of collisional orogens. *Earth Planet. Sci. Lett.* **1995**, *129*, 85–102. [CrossRef]
102. Bonin, B. Do coeval mafic and felsic magmas in post-collisional to within-plate regimes necessarily imply two contrasting, mantle and crustal, sources? A review. *Lithos* **2004**, *78*, 1–24. [CrossRef]
103. Goldfarb, R.J.; Groves, D.I.; Gardoll, S. Orogenic gold and geologic time: A global synthesis. *Ore Geol. Rev.* **2001**, *18*, 1–75. [CrossRef]
104. Sillitoe, R.H. Porphyry copper systems. *Econ. Geol.* **2010**, *105*, 3–41. [CrossRef]
105. Thiéblemont, D.; Stein, G.; Lescuyer, J.L. Gisements épithermaux et porphyriques: La connexion adakite. *C. R. Acad. Sci.* **1997**, *325*, 103–109. [CrossRef]
106. Oyarzun, R.; Márquez, A.; Lillo, J.; López, I.; Rivera, S. Giant versus small porphyry copper deposits of Cenozoic age in northern Chile: Adakitic versus normal calc-alkaline magmatism. *Miner. Depos.* **2001**, *36*, 794–798. [CrossRef]
107. Hou, Z.Q.; Zeng, P.S.; Gao, Y.F.; Du, A.D.; Fu, D.M. Himalayan Cu–Mo–Au mineralization in the eastern Indo–Asian collision zone: Constraints from Re–Os dating of molybdenite. *Miner. Depos.* **2006**, *41*, 33–48. [CrossRef]

108. Groves, D.I.; Santosh, M.; Deng, J.; Wang, Q.F.; Yang, L.Q.; Zhang, L. A holistic model for the origin of orogenic gold deposits and its implications for exploration. *Miner. Depos.* **2020**, *55*, 275–292. [CrossRef]
109. Goldfarb, R.J.; Taylor, R.D.; Collins, G.S.; Goryachev, N.A.; Orlandini, O.F. Phanerozoic continental growth and gold metallogeny of Asia. *Gondwana Res.* **2014**, *25*, 48–102. [CrossRef]
110. Deng, J.; Wang, Q.F.; Li, G.J.; Hou, Z.Q.; Jiang, C.Z.; Danyushevsky, L. Cenozoic tectono-magmatic and metallogenic processes in the Sanjiang region, southwestern China. *Earth-Sci. Rev.* **2020**, *138*, 268–299.

Disclaimer/Publisher's Note: The statements, opinions and data contained in all publications are solely those of the individual author(s) and contributor(s) and not of MDPI and/or the editor(s). MDPI and/or the editor(s) disclaim responsibility for any injury to people or property resulting from any ideas, methods, instructions or products referred to in the content.